



2 DOCTORAL THESIS

4 Optimisation studies and background
5 estimation in searches for the supersymmetric
6 partner of the top quark in all-hadronic final
7 states with the ATLAS Detector at the LHC

9 *A thesis submitted in fulfillment of the requirements
10 for the degree of Doctor of Philosophy*

11 *in the*

12 Experimental Particle Physics Research Group
13 School of Mathematical and Physical Sciences

14 *Author:*
15 **Fabrizio MIANO**

Supervisor:
Dr. Fabrizio SALVATORE

23rd January 2018

Dedicated to my family.

Acknowledgments

¹⁸ Thanks to every single thing that went wrong. It made me stronger.

Statement

20 I, Fabrizio MIANO, hereby declare that this thesis, titled “Optimisation studies and back-
21 ground estimation in searches for the supersymmetric partner of the top quark in all-
22 hadronic final states with the ATLAS Detector at the LHC”, has not been and will not be,
23 submitted in whole or in part to another University for the award of any other degree.

24 *Brighton, 23rd January 2018*

University of Sussex
School of Mathematical and Physical Sciences
Experimental Particle Physics Research Group

Doctoral Thesis

30
31 Optimisation studies and background estimation in searches for
32 the supersymmetric partner of the top quark in all-hadronic final
33 states with the ATLAS Detector at the LHC

35 by Fabrizio MIANO

Abstract

This thesis presents searches for supersymmetry in $\sqrt{s} = 13$ TeV proton-proton collisions at the LHC using data collected by the ATLAS detector in 2015, 2016. Events with 4 or more jets and missing transverse energy were selected. Kinematic variables were investigated and optimisations were performed to increase the sensitivity to supersymmetric signals. Standard Model backgrounds were estimated by means of Monte Carlo simulations and data-driven techniques. Before analysing the data in the blinded signal regions the agreement between data and background predictions and the extrapolations from control and validation regions to signal regions were validated. The analysis yielded no significant excess in any of the analyses performed. Therefore limits were set and the results were interpreted as lower bounds on the masses of supersymmetric particles in various scenarios and models.

48 **Contents**

49	Introduction	1
50	1 The Standard Model and Supersymmetry	2
51	1.1 The Standard Model	2
52	1.1.1 Electroweak Symmetry Breaking and the Higgs mechanism	6
53	1.1.2 Limitations of the Standard Model	8
54	1.2 Introduction to Supersymmetry and the MSSM	10
55	1.2.1 Minimal Supersymmetric Standard Model	12
56	1.2.2 Phenomenology of Supersymmetry	14
57	2 The ATLAS Experiment at the LHC	19
58	2.1 The LHC	19
59	2.2 The ATLAS Detector	21
60	2.2.1 The Magnet System	23
61	2.2.2 The Inner Detector	24
62	2.2.3 The Calorimeters	27
63	2.2.4 The Muon Spectrometer	29
64	2.3 The ATLAS Trigger System	30
65	3 The ATLAS Trigger System	31
66	3.1 Overview	31
67	3.2 Level-1 Trigger	32
68	3.3 High-Level Trigger	35
69	3.3.1 Inner detector tracking	35
70	3.3.2 Performance of HLT	36
71	4 Event Simulation and Object Reconstruction	42
72	4.1 Generation of a MC-simulated event	42
73	4.1.1 Detector simulation	47
74	4.2 Object Reconstruction	47
75	4.3 Object Selection	48
76	4.3.1 Baseline Object Selection	48

77	4.3.2 Overlap Removal	48
78	4.3.3 Signal Object Selection	48
79	5 Stop searches in final states with jets and missing transverse energy	49
80	6 Results and Statistical Intepretations	50
81	Appendix title	51
82	Acronyms	52
83	Bibliography	55

⁸⁴ Introduction

⁸⁵ Last thing to write

86 1 | The Standard Model 87 and Supersymmetry

88

A theory is something nobody believes, except the person who made it. An experiment is something everybody believes, except the person who made it.

Albert Einstein

89 Section 1.1 presents an overview of the Standard Model (**SM**) of particle physics, to-
 90 gether with its limitations (Section 1.1.2) and the need of an extension. One of the most
 91 popular of these extensions, Supersymmetry (**SUSY**), will be discussed in Section 1.2
 92 where an overview of the theory and the motivations behind its success, will be presen-
 93 ted. The description of the Minimal Supersymmetric Standard Model (**MSSM**) in Sec-
 94 tion 1.2.1, and finally the phenomenology of supersymmetry, with particular attention to
 95 third-generation supersymmetry (as the most relevant theoretical support to the analyses
 96 presented in this work) will be discussed in Section 1.2.2.

97 1.1 The Standard Model

98 The **SM** is an effective theory that aims to provide a general description of fundamental
 99 particles and their interactions.

100 The 20th century can be considered a quantum revolution. Several experiments led to
 101 discoveries which were found to be, together with the formalised theory, a solid base of
 102 the **SM** of particle physics and our description of nature. Several particles were first pre-
 103 dicted and then experimentally observed e. g. the W and the Z bosons, the τ lepton, [1],
 104 and more recently the Higgs boson at the Large Hadron Collider (**LHC**) discovered by
 105 the **ATLAS** [2] and **CMS** [3] collaborations.

106 The **SM** is a Quantum Field Theory (**QFT**) where particles are treated like excitations
 107 of quantum fields in a four-dimensional Minkowski spacetime [4]. It can describe three
 108 of the four fundamental forces; weak, electromagnetic, and strong, but not gravity.

The most general classification of the elementary particles within the SM can be made by means of spin and their behaviour under Poincaré transformations [5]: *fermions* (leptons and quarks), usually referred to as matter particles, which have half-integer spin values, in unit of \hbar , and *bosons*, usually referred to as information carriers, which have integer-spin values. A noteworthy subset of bosons is formed by the Spin-1 bosons, also known as gauge bosons. These can be considered mediators of the forces. Figure 1.1 displays the elementary particles of the Standard Model known as of today.

Symmetries and Gauge Groups

In 1915, the German mathematician and theoretical physicist Emmy Noether (23 March 1882 – 14 April 1935) proved that every differentiable symmetry of the action - defined as the integral over space of a Lagrangian density function $S = \int \mathcal{L} dt$ - of a physical system has a corresponding conservation law [6]. More generally, a symmetry is a property of a physical system and under certain transformations this property is preserved.

A gauge theory in QFT, is a theory in which the Lagrangian is invariant under a continuous group of local transformations. Group theory was adopted to describe the symmetries conserved in the SM. The gauge group of the SM is the *Lie Group* which contains all the transformations between possible gauges [5]. The Lie algebra of group generators is associated to any Lie group and for each group generator there emerges a corresponding field, called the gauge field, and the quanta of such fields are called *gauge bosons*.

The three SM interactions can therefore be mathematically described by the following:

$$U(1)_Y \otimes SU(2)_L \otimes SU(3)_C \quad (1.1)$$

Here, Y is the weak hypercharge, used to estimate the correlation between the electric charge (Q) and the third component of the weak isospin (I_3) via the relation $Q = I_3 + Y/2$, where I_3 can either be $\pm 1/2$ or 0 for left-handed and right-handed particles, respectively, and C the colour charge, L the left-handedness.

Quantum Electrodynamics (QED) is an Abelian gauge theory described by the sym-

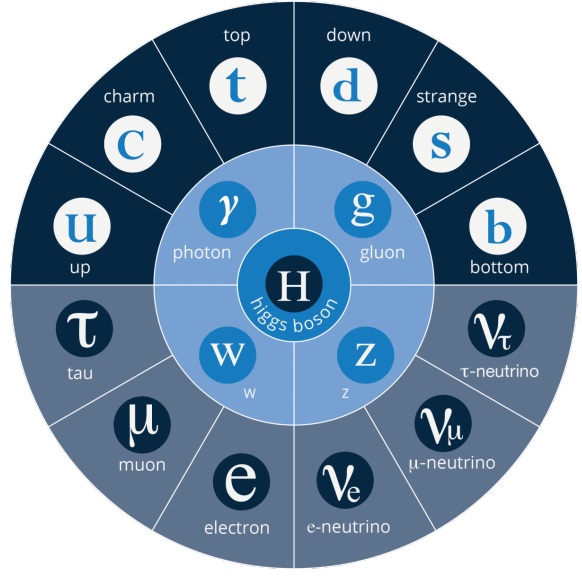


Figure 1.1: The elementary particles of the SM. From the outermost to the innermost; fermions (quarks, top-half wheel, leptons, bottom-half wheel), vector bosons, and the Higgs boson.

¹⁴⁵ metry group $U(1)$. The electromagnetic four-potential is its gauge field and the photon
¹⁴⁶ its gauge boson [7]. The interactions between charged fermions occurs by the exchange
¹⁴⁷ of a massless photon.

¹⁴⁸ The weak interaction is described by the non-Abelian gauge group $SU(2)$. The $SU(2)$
¹⁴⁹ generators are the massless gauge bosons $W_\mu^{\alpha=1,\dots,3}$ and they violate the parity by acting
¹⁵⁰ only on left-handed particles. As a consequence of non-Abelianity, $SU(2)$ gauge bosons
¹⁵¹ can self-interact as the generator commutators are non-vanishing. Additionally, quarks
¹⁵² can also interact through weak interaction as mixtures of **SM** eigenstates as described by
¹⁵³ the CKM matrix [8].

¹⁵⁴ Finally, the strong interaction, described by the symmetry group $SU(3)$, has eight
¹⁵⁵ massless gauge bosons, the gluons, $G_\mu^{\alpha=1,\dots,8}$ which can be exchanged between quarks
¹⁵⁶ and can also self-interact.

¹⁵⁷ Fermions

¹⁵⁸ There are twelve fermions in the **SM**: six quarks and six leptons. In particular, fermions
¹⁵⁹ can be grouped into three generations. Each generation contains four particles; one up-
¹⁶⁰ and one down-type quark, one charged lepton and one neutral lepton. The masses of the
¹⁶¹ charged leptons and quarks increase with the generation. The six quarks of the **SM** can
¹⁶² be grouped into three $S(2)$ doublets;

$$\begin{pmatrix} u \\ d \end{pmatrix}, \quad \begin{pmatrix} c \\ s \end{pmatrix}, \quad \begin{pmatrix} t \\ b \end{pmatrix}$$

¹⁶³ The up-type quarks (*up, charm, top*) have charge $+\frac{2}{3}e$ and the down-type quarks (*down,*
¹⁶⁴ *strange, beauty/bottom*) have charge $-\frac{1}{3}e$, where e is the electron charge. Quarks also have
¹⁶⁵ another quantum number that can be seen as the analogue of the electric charge; the col-
¹⁶⁶ our charge. This can exist in three different states; *red, green* and *blue*, but they cannot
¹⁶⁷ exist as free particles. They rather group to form hadronic matter, also known as *had-*
¹⁶⁸ *rtons*. There are two kinds of hadrons; mesons and baryons. Mesons are quark-antiquark
¹⁶⁹ systems, e.g. the pion, and baryons are three-quark system, e.g. protons and neutrons.
¹⁷⁰ Quarks and anti-quarks have a baryon number of $\frac{1}{3}$ and $-\frac{1}{3}$, respectively.

¹⁷¹ There are six leptons and they can be classified in charged leptons (electron e , muon
¹⁷² μ , tau τ) and neutral leptons (electron neutrino ν_e , muon neutrino ν_μ , tau neutrino ν_τ).

$$\begin{pmatrix} \nu_e \\ e^- \end{pmatrix}, \quad \begin{pmatrix} \nu_\mu \\ \mu^- \end{pmatrix}, \quad \begin{pmatrix} \nu_\tau \\ \tau^- \end{pmatrix}$$

¹⁷³ Each lepton has a characteristic quantum number, called lepton number (L). Negat-
¹⁷⁴ ively (positively) charged leptons have $L = -1$ ($L = 1$) and neutral leptons have $L = 1$.
¹⁷⁵ The lepton number is conserved in all the interactions.

176 Forces of Nature

177 Forces in the **SM** are described by gauge theories, where the interactions are mediated by
 178 a vector gauge boson.

179 **QED** describes the electromagnetic force, which only affects charged leptons (neut-
 180 rinos are instead affected by the weak force, mediated by the W^\pm and Z^0 bosons) and
 181 quarks and it is mediated by the photon (γ).

182 The weak interaction is associated with handedness (the projection of a particle spin
 183 onto its direction of motion). Both leptons and quarks have left- and right-handed com-
 184 ponents. However, only the left-handed (right-handed) component for neutrinos (anti-
 185 neutrinos) has been observed. This means that nature prefers to produce left-handed
 186 neutrinos and right-handed anti-neutrinos, which is the so-called *parity violation* [9].

187 The strong interaction, mediated by the gluon, electrically neutral and massless, is
 188 described by Quantum Chromo Dynamics (**QCD**). Its coupling (α_s) increases with in-
 189 creasing distance and is smaller at short range. In particular, α_s evolves as a function of
 190 the transferred four-momentum squared, Q^2 , as follows:

$$\alpha_s(Q^2) \propto \frac{1}{n_f \log\left(\frac{Q^2}{\Lambda_{\text{QCD}}^2}\right)} \quad (1.2)$$

191 where n_f is the number of quarks with mass below Q^2 and Λ_{QCD} is the **QCD** character-
 192 istic scale. Eq. 1.2 shows that α_s decreases as a function of Λ_{QCD} , but at the same time it
 193 quickly diverges when Q^2 gets closer to Λ . In other words, as the condition $\alpha_s \ll 1$ only
 194 holds for $Q^2 \gg \Lambda_{\text{QCD}}$, **QCD** can be treated perturbatively¹ only at high energy scales².
 195 Furthermore, **QCD** has three important features:

- 196 • *confinement*: quarks or gluons cannot be observed as free particles, but only col-
 197 ourless “singlet” states can be observed as “jets”, namely collimated cone-shaped
 198 sprays of hadrons;
- 199 • *asymptotic freedom*: interactions between quarks and gluons become weaker as the
 200 energy scale increases and the corresponding length scale decreases, as $\alpha_s \rightarrow 0$ for
 201 $Q^2 \rightarrow \infty$
- 202 • *hadronisation*: when quarks or gluons are pulled apart, the production of pairs of
 203 hadrons, produced from the vacuum, is energetically preferred to an increase in
 204 distance.

205 Table 1.1 summarises the forces described in the **SM** and the main characteristics of
 206 the mediators. The gravitational force is believed to be mediated by the graviton, but as
 207 already mentioned, since it is not included in the **SM**, it will not be further discussed.

¹ Perturbation theory (quantum mechanics) is an approximation to describe a complicated quantum system in terms of a simpler one.

² Perturbation theory can only be used when the coupling constant (expansion parameter) is small.

Table 1.1: Forces and mediators described by the SM

Force	Name	Symbol	Mass [GeV]	Charge
Electromagnetic	Photon	γ	0	0
Weak	W	W^\pm	80.398	$\pm e$
	Z	Z^0	91.188	0
Strong	Gluon	g	0	0

208 **1.1.1 Electroweak Symmetry Breaking and the Higgs mechanism**

209 In 1979 Sheldon Glashow, Abdus Salam, and Steven Weinberg were awarded the Nobel
 210 Prize in Physics for their contributions to the so-called electroweak unification [10, 11, 12].
 211 In the mathematical description of the SM in 1.1, the electroweak interaction is described
 212 by $U(1)_Y \otimes SU(2)_L$.

213 The four electroweak physical bosons W^\pm , Z and γ are related to the four unphysical
 214 gauge bosons $W_\mu^{\alpha=1,\dots,3}$ and B_μ . In particular, to obtain the physical bosons the gauge
 215 bosons have to mix as follows;

$$A_\mu = W_\mu^3 \sin \theta_W + B_\mu \cos \theta_W \quad (1.3)$$

216

$$Z_\mu = W_\mu^3 \cos \theta_W - B_\mu \sin \theta_W \quad (1.4)$$

217

$$W_\mu^\pm = \frac{1}{\sqrt{2}} (W_\mu^1 \mp i W_\mu^2) \quad (1.5)$$

218 Here, θ_W is the so-called *Weinberg angle* which is the angle by which spontaneous sym-
 219 metry breaking rotates the original gauge bosons W_μ^3 and B_μ into the physical Z and γ .
 220 A_μ and Z_μ are the photon and the Z boson fields, respectively. The θ_W angle can be ex-
 221 perimentally determined in terms of the coupling strengths, of the $B_\mu(g_1)$ and the $W_\mu^\alpha(g_2)$
 222 to the fermions, using the relation $\tan \theta_W = g_1/g_2$.

223 The mass terms for both gauge bosons and fermionic fields are forbidden by the elec-
 224 troweak gauge as they are not invariant under gauge transformations. Nonetheless, it
 225 was experimentally proven that W and Z bosons are massive [7], therefore in order for
 226 the SM assumption to hold, the electroweak symmetry must be broken.

227 The SM Lagrangian can be written as the sum of the various Lagrangians describing
 228 the three interactions and the masses of the elementary particles as follows:

$$\mathcal{L}_{\text{SM}} = \mathcal{L}_{\text{EWK}} + \mathcal{L}_{\text{QCD}} + \mathcal{L}_{\text{Mass}} \quad (1.6)$$

229 In order for the SM Lagrangian to remain a renormalisable theory, the mass terms ($\mathcal{L}_{\text{Mass}}$)
 230 cannot be insterted by hand. A mechanism, that can preserve the gauge symmetry in the
 231 SM and can solve the inconsistency arisen from the mass difference between the gauge

²³² bosons and the physical ones is needed. A British theoretical physicist, Peter Higgs (29
²³³ May 1929, Newcastle upon Tyne, UK), came up with a brilliant solution for which he was
²³⁴ awarded the Nobel Prize in Physics in 2013. Higgs proposed [13] that broken symmetry
²³⁵ in the electroweak theory could explain the origin of masses of elementary particles, and
²³⁶ in particular of W and Z bosons. The mechanism introduces a scalar field, known as the
²³⁷ Higgs field, thought to couple to both massive fermions and bosons. The $SU(2)$ doublet
²³⁸ is then introduced in the **SM**;

$$\phi = \begin{pmatrix} \phi^+ \\ \phi^0 \end{pmatrix} \quad (1.7)$$

²³⁹ with ϕ^+ and ϕ^0 generic complex fields:

$$\phi^+ = \frac{\phi_1 + i\phi_2}{\sqrt{2}}, \quad \phi^0 = \frac{\phi_3 + i\phi_4}{\sqrt{2}} \quad (1.8)$$

²⁴⁰ Consider a Lagrangian of the form:

$$\mathcal{L}_{\text{Higgs}} = (\partial_\mu \phi)^* (\partial^\mu \phi) - V(\phi) \quad (1.9)$$

²⁴¹ Renormalizability and $SU(2)_L \otimes U(1)_Y$ invariance require the Higgs potential to be of the
²⁴² following form:

$$V(\phi) = \mu^2 \phi^\dagger \phi + \lambda \left(\phi^\dagger \phi \right)^2 \quad (1.10)$$

²⁴³ The Lagrangian in Eq. 1.9 is the Higgs Lagrangian if ϕ is chosen to be the following:

$$\phi = \begin{pmatrix} \phi^+ \\ \phi^0 \end{pmatrix} = \begin{pmatrix} G^+ \\ \frac{1}{\sqrt{2}} (v + H + iG^0) \end{pmatrix}$$

²⁴⁴ Here, the complex scalar field G^\pm and the real scalar field G^0 correspond to Goldstone
²⁴⁵ bosons, and the real scalar field H is the **SM** Higgs boson field [14]. These massless scalars
²⁴⁶ are absorbed due to the gauge transformations by the electroweak gauge bosons of the
²⁴⁷ **SM**:

$$\phi = \begin{pmatrix} \phi^+ \\ \phi^0 \end{pmatrix} = \begin{pmatrix} 0 \\ \frac{1}{\sqrt{2}} (v + H) \end{pmatrix} \quad (1.11)$$

²⁴⁸ The Higgs potential in Eq. 1.10 is displayed in Fig. 1.2 if λ and μ are chosen to be
²⁴⁹ real. Such potential has a non-zero ground state, v , also known as Vacuum Expectation
²⁵⁰ Value (**VEV**):

$$\phi_0 = \begin{pmatrix} 0 \\ \frac{1}{\sqrt{2}} v \end{pmatrix} \quad (1.12)$$

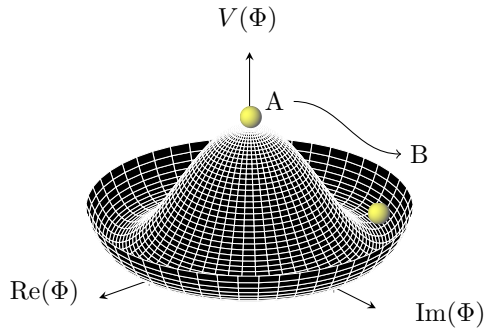


Figure 1.2: The Higgs potential in the complex plane.

- 251 Such representation remains invariant under $U(1)$ allowing electric charge conservation.
 252 However, the **SM** gauge symmetry 1.1 is broken into $SU(2)_L \otimes U(1)_Y$.

253 In summary, to generate particle masses gauge symmetry must be broken. How-
 254 ever, in order for the theory to remain renormalisable, the global Lagrangian symmetry
 255 must be preserved. This can be solved introducing the concept of *spontaneous* symmetry
 256 breaking (SSB): a mechanism that allows a symmetric Lagrangian, but not a symmet-
 257 ric vacuum. In particular, given a Lagrangian invariant under a certain transformation,
 258 T_X , and a generic set of states, that transform under T_X as the elements of a multiplet,
 259 the symmetry is spontaneously broken if one of those states is arbitrarily chosen as the
 260 ground state of the system. The interaction of the Higgs field with the $SU(2) \otimes U(1)$
 261 gauge fields, $W_\mu^{\alpha=1,2,3}$, result in the three gauge bosons fields acquiring mass whilst the
 262 A_μ field remains massless.

263 1.1.2 Limitations of the Standard Model

264 The **SM** has been extensively validated at the Large Electron-Positron Collider (**LEP**)
 265 (European Organization for Nuclear Research (**CERN**)) first. Run 1 of the **LHC** exten-
 266 ded the validation beyond the energy limits of LEP (200 GeV) as shown in Fig. 1.3: the
 267 agreement, between the measured production cross-section of various **SM** processes and
 268 the **SM** predictions, looks very good. However, there are some fundamental questions
 269 that still have no answer.

270 Hierarchy Problem

271 Due to the coupling of the Higgs field to the fermionic fields, the one-loop corrections to
 272 the Higgs mass receive several contributions [16]. In particular, looking at Fig. 1.4:

$$\Delta m_H^2 = -\frac{|\lambda_f|^2}{8\pi^2} \Lambda_{\text{UV}}^2 + \dots \quad (1.13)$$

273 where, λ_f is the coupling constant to the fermionic field; Δm_H^2 is the difference between
 274 the observed Higgs mass m_H^2 and the bare mass, m_H^0 (Lagrangian parameter); Λ_{UV} is the

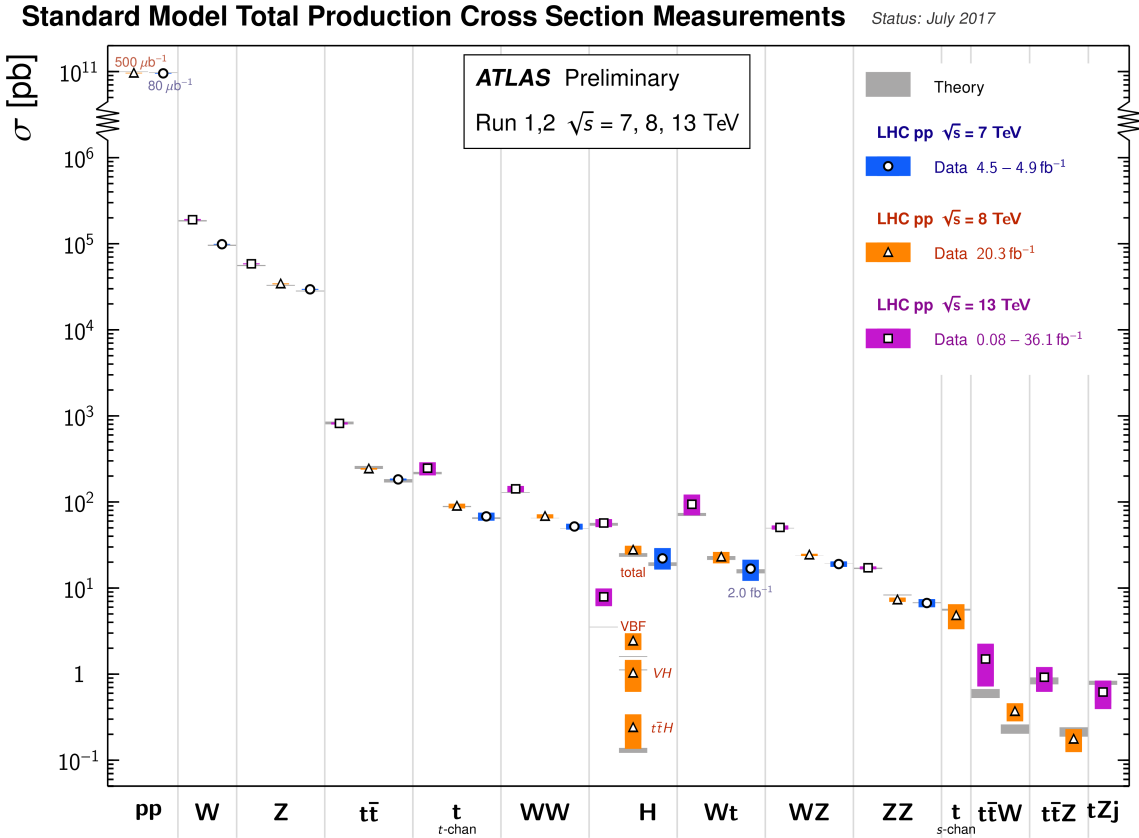


Figure 1.3: Summary of several SM total production cross-section measurements, corrected for leptonic branching fractions, compared to the corresponding theoretical expectations. All theoretical expectations were calculated at NLO or higher. The luminosity used for each measurement is indicated close to the data point. Uncertainties for the theoretical predictions are quoted from the original ATLAS papers. They were not always evaluated using the same prescriptions for PDFs and scales. Not all measurements are statistically significant yet [15].

275 ultraviolet momentum cut-off, selected to be at the Planck scale ($\sim 2 \cdot 10^{18}$ GeV), at which
 276 a QFT description of gravity is believed to become possible. The correction to the Higgs
 277 mass will be around 30 orders of magnitude larger than Higgs mass itself, in opposition
 278 to what has been measured. This difference just mentioned, between the electroweak
 279 scale and the Planck scale arisen from the quantum corrections to the Higgs mass, is the
 280 so-called Hierarchy Problem [16].

281 Neutrino Masses

282 The Super-Kamiokande Collaboration in 1998 [17], and SNO Collaboration in 2001 [18],
 283 have provided measurements of the neutrino flux from solar and atmospheric sources.
 284 The Nobel Prize in Physics 2015 was awarded jointly to Takaaki Kajita and Arthur B.
 285 McDonald “for the discovery of neutrino oscillations, which shows that neutrinos have
 286 mass” [19]. Such feature contradicts the description of the neutrinos in the SM, which are
 287 assumed to be massless, therefore there needs to be a mechanism that generates neutrino
 288 masses. One possibility would be to add Majorana mass terms or adding additional

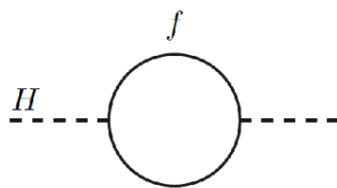


Figure 1.4: One-loop quantum corrections to the Higgs mass. A fermion correction with coupling λ_f .

289 right-handed neutrinos with a very heavy mass, known as the see-saw mechanism [20].

290 Dark Matter

291 Although Dark Matter (DM) has never been directly observed, its existence is inferred
292 from its gravitational effects. For example, looking at galaxies rotation, it was observed
293 that the rotation speed was higher than expected, given the amount of visible matter [21].
294 Two different reasoning arose during the last century to justify such effect: there is either
295 matter that cannot be seen by us (in terms of visible light), which contributes to the gal-
296 atcis mass, or the general relativity works differently at galactic distances. The former
297 is believed to be the most likely and it implies the existence of new particles which
298 do not interact via electromagnetic interaction, the so-called Weakly Interacting Massive
299 Particle (WIMP) [22].

300 1.2 Introduction to Supersymmetry and the MSSM

301 One of the main motivations for SUSY is the cancellation of quadratic divergences to
302 Δm_H^2 via the introduction of the so-called SUSY particles with a half-integer spin differ-
303 ence with respect to their SM partners. This provides a solution to the hierarchy problem
304 as the Higgs mass squared potential receives corrections from a new scalar of mass of the
305 form:

$$\Delta m_H^2 = -\frac{|\lambda_S|^2}{16\pi^2} \left[\Lambda_{UV}^2 - 2m_S^2 \ln(\Lambda_{UV}/m_S) + \dots \right] \quad (1.14)$$

306 where, λ_S is the coupling of SUSY particles to the Higgs field. This term cancels the
307 fermionic contributions in Eq. 1.13 since the couplings are the same, which means that
308 the experimentally measured mass of the Higgs boson can be obtained without perform-
309 ing any unnatural *tuning* of the parameters [23, 24]. This is what makes SUSY a *natural*
310 theory³.

311 The running of gauge coupling constants⁴ is predicted by the SM, but, as previously
312 mentioned, although the electroweak unification occurs at ~ 100 GeV, it is not the case

³ The Naturalness of a theory is a property for which dimensionless ratios between free parameters should assume sensible values and that free parameters are not fine-tuned.

⁴ The coupling strength, as a function of energy, is calculable given a value at a fixed scale.

for the strong force. In the **MSSM**, a supersymmetric extension of the **SM**, due to addition of *new* particles involved in the gauge interactions, a new set of coefficients arise. As shown in Fig. 1.5 the three lines, representing electromagnetic (dashed blue), weak (dashed red) and strong (solid green) interactions respectively, do not meet at one point, but they do with the introduction of supersymmetry. This can therefore be considered an approximate unification, of all three gauge couplings, at the Planck scale, which is an indication for a potential Grand Unification Theory (**GUT**) that could be obtained within a supersymmetric model. In addition, together with the unification at the **GUT** scale, another good motivation for **SUSY** searches is that, if **SUSY** is **MSSM**-like (m_{SUSY} not heavier than ~ 1 TeV), it can be discovered at the **LHC**.

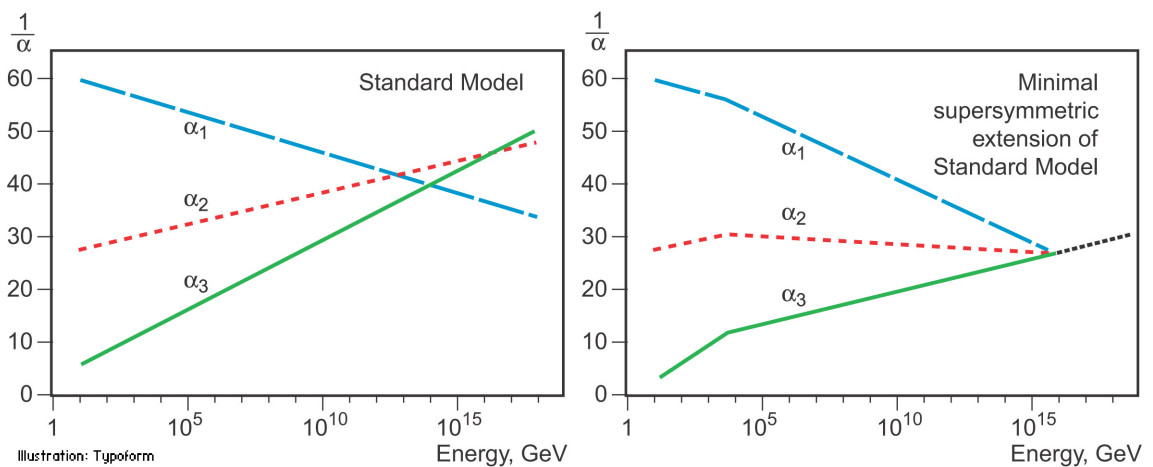


Figure 1.5: The inverse couplings of electromagnetic (dashed blue), weak (dashed red) and strong (solid green) interactions with the **SM** (left) and a supersymmetric model (right). In the **SM** the three lines do not meet at one point, but with the introduction of supersymmetry, and assuming that the supersymmetric particles are not heavier than about 1 TeV, they do meet.

SUSY introduces a space-time symmetry that relates bosons to fermions and vice-versa, via a transformation of the form of:

$$Q |\text{fermion}\rangle = |\text{boson}\rangle, \quad Q |\text{boson}\rangle = |\text{fermion}\rangle \quad (1.15)$$

For each **SM** particle there exists a supersymmetric partner, generally called *sparticle* (where the s stands for “scalar”), with a spin difference of $\Delta s = 1/2$. Each pair of partners is arranged in a so-called *supermultiplet*. The two components have same masses and quantum numbers, but different spin, due to their relation to the Q operator (and its properties).

Sleptons and *squarks* interact as their **SM** equivalent, namely for example, the superpartners of the left-handed paragraph* fermion components couple weakly, while the superpartners of the right-handed **SM** fermion components do not. Gauge supermultiplets contain a vector boson and two spin- $\frac{1}{2}$ fermions. Spin-1 bosons are arranged in gauge multiplets, and their superpartners, referred to as *gauginos*, are spin- $\frac{1}{2}$ fermions. Unlike

335 the **SM**, the Spin-0 Higgs boson has two supermultiplets containing sparticles with dif-
 336 ferent weak isospin values, referred to as H_u and H_d , which are required to give mass to
 337 both the up- and down-type sparticles. Higgs **SUSY** partners are called the *Higgsinos*.

338 As of today, **SUSY** particles have not been observed, resulting in the assumption that
 339 **SUSY** must be a broken symmetry, otherwise superpartners would have the same masses
 340 as their **SM** equivalent. However, if sparticles were to be too heavy (close to the Planck
 341 scale), the hierarchy problem would be re-introduced and therefore would still remain
 342 unsolved. The *soft* **SUSY** breaking mechanism, described in Section 1.2.1, overcomes this
 343 problem by imposing constraints on the masses of sparticles to a range that can be exper-
 344 imentally explored.

345 1.2.1 Minimal Supersymmetric Standard Model

346 There does not exist a unique extension of a supersymmetric **SM**, i. e. **SUSY** is not a well-
 347 defined model but it is more a framework within which various **SM** extensions can be
 348 derived. The **MSSM**, a minimal supersymmetric extension of the **SM** [25], is defined by
 349 essentially doubling up the number of particles in the **SM** theory in order to include all
 350 the **SM** particles as well as their corresponding superpartners.

351 Soft SUSY breaking

352 The mass spectrum of the **SUSY** particles must sit somewhere at a larger scale than the
 353 **SM** one, as supersymmetric particles have not been discovered at the mass scale of their
 354 **SM** partners. This gives us a hint that supersymmetry cannot be an exact symmetry and
 355 therefore it is broken. There has to be an analogy with the electroweak symmetry break-
 356 ing discussed in 1.1.1, where the symmetry is broken by a non-zero **VEV**. The mechanism
 357 must be spontaneous in order for the broken supersymmetry to still provide a solution
 358 to the hierarchy problem: a big alteration of the relationship between the fermionic and
 359 scalar couplings will result in a non-cancellation of the corrections to the Higgs mass
 360 squared parameter. This equates to adding terms to the **SUSY** Lagrangian which are
 361 gauge invariant and violate **SUSY**, but contain only masses and couplings with positive
 362 mass dimension. The total Lagrangian is defined as;

$$\mathcal{L}_{\text{MSSM}} = \mathcal{L}_{\text{SUSY}} + \mathcal{L}_{\text{soft}} \quad (1.16)$$

363 where all the additional terms are contained within $\mathcal{L}_{\text{soft}}$ and the original **SUSY** invariant
 364 interaction terms are contained within $\mathcal{L}_{\text{SUSY}}$. A new set of parameters is then introduced
 365 into this **SM** extension. These parameters determine the mixing between the flavour
 366 eigenstates and the **SUSY** phenomenology, which will be discussed in Section 1.2.2.

367 **MSSM mass spectrum**

368 As per the **SM** gauge bosons, the gaugino masses are affected by electroweak symmetry
 369 breaking. The new states, introduced in the $\mathcal{L}_{\text{soft}}$, mix to form the mass eigenstates of
 370 the sparticles. The neutral Winos, \tilde{W}^0 , Binos, \tilde{B}^0 and higgsinos \tilde{H}^0 mix to form the four
 371 *neutralinos* $\tilde{\chi}_i^0$ ($i = 1, 2, 3, 4$) as follows;

$$\begin{pmatrix} \tilde{\chi}_1^0 \\ \tilde{\chi}_2^0 \\ \tilde{\chi}_3^0 \\ \tilde{\chi}_4^0 \end{pmatrix} = \begin{pmatrix} M_1 & 0 & -c_\beta s_W m_Z & c_W s_\beta m_Z \\ 0 & M_2 & c_\beta c_W m_Z & -c_W s_\beta m_Z \\ -c_\beta s_W m_Z & c_\beta s_W m_Z & 0 & -\mu \\ s_\beta c_W m_Z & -s_\beta c_W m_Z & -\mu & 0 \end{pmatrix} \begin{pmatrix} \tilde{B}^0 \\ \tilde{W}^0 \\ \tilde{H}_u^0 \\ \tilde{H}_d^0 \end{pmatrix} \quad (1.17)$$

372 Here, $c_\beta = \cos \beta$, $(s_\beta) = \sin \beta$, $c_W = \cos \theta_W$ and $(s_W) = \sin \theta_W$. M_1, M_2 are related to
 373 gaugino masses and μ to higgsino mass, $\tan \beta$ is the ratio of the **VEVs** of the two Higgs
 374 doublet fields, θ_W is the ratio of the electroweak coupling constants and, m_Z (m_W) is the
 375 mass of the Z (W) boson. The neutralino indeces are conventionally assumed to increase
 376 with their masses. The charged winos \tilde{W}^\pm and higgsinos \tilde{H}^\pm mix to form four *charginos*,
 377 $\tilde{\chi}_i^\pm$ ($i = 1, 2$) as it follows;

$$\begin{pmatrix} \tilde{\chi}_1^\pm \\ \tilde{\chi}_2^\pm \end{pmatrix} = \begin{pmatrix} M_2 & \sqrt{2}m_W s_\beta \\ \sqrt{2}m_W c_\beta & \mu \end{pmatrix} \begin{pmatrix} \tilde{W}^\pm \\ \tilde{H}^\pm \end{pmatrix} \quad (1.18)$$

378 Charginos and neutralinos mix as described in Eq. 1.18 and 1.17 and will be referred
 379 to as bino-like, wino-like or higgsino-like depending on their phenomenology. Gluinos
 380 do not mix as they carry colour charge.

381 The Higgs sector is also affected. There are five mass eigenstates, h^0, H^0, A^0 , and H^\pm .
 382 These, together with the other **MSSM** particles are listed in Table 1.2.

Table 1.2: **SUSY** particles in the **MSSM**

Name	Spin	Gauge Eigenstates	Mass Eigenstates
Squarks (\tilde{q})	0	$\tilde{u}_L \tilde{u}_R \tilde{d}_L \tilde{d}_R$	(same)
		$\tilde{c}_L \tilde{c}_R \tilde{s}_L \tilde{s}_R$	(same)
		$\tilde{t}_L \tilde{t}_R \tilde{b}_L \tilde{b}_R$	$\tilde{t}_1 \tilde{t}_2 \tilde{b}_1 \tilde{b}_2$
Sleptons (\tilde{l})	0	$\tilde{e}_L \tilde{e}_R \tilde{\nu}_L$	(same)
		$\tilde{\mu}_L \tilde{\mu}_R \tilde{\nu}_L$	(same)
		$\tilde{\tau}_L \tilde{\tau}_R \tilde{\nu}_\tau$	$\tilde{\tau}_1 \tilde{\tau}_2 \tilde{\nu}_\tau$
Higgs bosons	0	$H_u^0 H_d^0 H_d^+ H_d^-$	$h^0 H^0 A^0 H^\pm$
Neutralinos ($\tilde{\chi}_j^0$)	1/2	$\tilde{B}^0 \tilde{W}^0 \tilde{H}_u^0 \tilde{H}_d^0$	$\tilde{\chi}_1^0 \tilde{\chi}_2^0 \tilde{\chi}_3^0 \tilde{\chi}_4^0$
Charginos ($\tilde{\chi}_i^\pm$)	1/2	$\tilde{W}^\pm \tilde{H}_u^+ \tilde{H}_u^-$	$\tilde{\chi}_1^\pm \tilde{\chi}_2^\pm$
Gluino	1/2	\tilde{g}	(same)
Gravitino	3/2	\tilde{G}	(same)

In the **MSSM** the squark sector is specified by the mass matrix in the basis $(\tilde{q}_L, \tilde{q}_R)$ with $\tilde{q} = \tilde{t}$ or \tilde{b} [26]. A rotation matrix can be defined also for left- and right-handed squarks and sleptons, although in the **MSSM** the mixing is assumed to be non-zero only for the third-generation scalar partners. Stop, \tilde{t}_L, \tilde{t}_R , sbottom \tilde{b}_L, \tilde{b}_R , and stau, $\tilde{\tau}_L, \tilde{\tau}_R$ rotate into mass eigenstates, $\tilde{t}_1, \tilde{t}_2, \tilde{b}_1, \tilde{b}_2, \tilde{\tau}_1, \tilde{\tau}_2$, respectively, as described in Eq. 1.19 [27].

$$\mathcal{M}_{\tilde{q}}^2 = \begin{pmatrix} m_{\tilde{q}_L}^2 & a_q m_q \\ a_q m_q & m_{\tilde{q}_R}^2 \end{pmatrix} \quad (1.19)$$

with

$$\begin{aligned} m_{\tilde{q}_L}^2 &= M_{\tilde{Q}}^2 + m_Z^2 \cos 2\beta \left(I_3^{q_L} - e_q \sin^2 \theta_W \right) + m_q^2, \\ m_{\tilde{q}_R}^2 &= M_{\{\tilde{U}, \tilde{D}\}}^2 + m_Z^2 \cos 2\beta e_q \sin^2 \theta_W + m_q^2, \\ a_q m_q &= \begin{cases} (A_t - \mu \cot \beta) m_t, & (\tilde{q} = \tilde{t}) \\ (A_b - \mu \tan \beta) m_t, & (\tilde{q} = \tilde{b}) \end{cases} \end{aligned} \quad (1.20)$$

Here, $I_3^{q_L}$ is the third component of the weak isospin and e_q the electric charge of the quark q . $M_{\{\tilde{Q}, \tilde{U}, \tilde{D}\}}$ and $A_{t,b}$ are soft **SUSY**-breaking parameters, μ is the higgsino mass parameter, and $\tan \beta$, as previously mentioned, is the ratio of Higgs field **VEVs**. By diagonalising the matrix in Eq. 1.19 one gets the mass eigenstates

$$\tilde{q}_1 = \tilde{q}_L \cos \theta_{\tilde{q}} + \tilde{q}_R \sin \theta_{\tilde{q}}$$

$$\tilde{q}_2 = -\tilde{q}_L \sin \theta_{\tilde{q}} + \tilde{q}_R \cos \theta_{\tilde{q}}$$

with the mass eigenvalues $m_{\tilde{q}_1}, m_{\tilde{q}_2}$ ($m_{\tilde{q}_1} < m_{\tilde{q}_2}$) and the mixing angle $\theta_{\tilde{q}}$ ($-\pi/2 < \theta_{\tilde{q}} \leq \pi/2$).

1.2.2 Phenomenology of Supersymmetry

As previously mentioned, the introduction of **SUSY** particles overcomes the problem of an unnatural fine-tuning to the Higgs mass due to its quadratic corrections.

R-parity

The most general **MSSM** can contain operators that violate baryon and/or lepton number, thus allowing proton decays. The non-observation of proton decays forbids the existence of such terms. A possibility to avoid these operators is to introduce a new discrete symmetry named *R*-parity. The conserved quantum number is defined as;

$$P_R = (-1)^{3(B-L)+2s} \quad (1.21)$$

where B, L , and s are the baryon, lepton, and spin number, respectively.

403 The **SM** particles have $R = 1$ and **SUSY** partners have $R = -1$. When R -parity
 404 conservation is imposed on **MSSM** models, the mixing between particles and sparticles
 405 cannot occur, resulting in the number of **SUSY** particles to be even at every interaction
 406 vertex. Furthermore, all sparticles must be pair-produced and the Lightest Stable Particle
 407 (**LSP**) has to be stable and can be a good Dark Matter candidate.

408 Although **SUSY** searches in an R -Parity Violating (**RPV**) scenario have been exten-
 409 sively investigated by the particle-physics community, in this work only R -Parity Con-
 410 serving (**RPC**) models, where the $\tilde{\chi}_1^0$ is assumed to be the **LSP**, were considered.

411 **Phenomenological MSSM (pMSSM)**

412 As mentioned in 1.2.1, once the **SUSY** soft breaking occurred, the unconstrained **MSSM**
 413 has more than 100 parameters in addition to the **SM** ones. This makes the **SUSY** searches,
 414 e. g. finding regions, in parameter space, that are consistent with the data, rather imprac-
 415 tical. However, the number of free parameters can be reduced down to 19 if the following
 416 assumptions are made;

- 417 • no new source of CP-violation (CKM matrix is the only source)
- 418 • no Flavour Changing Neutral Currents (**FCNC**)
- 419 • masses of the first- and second-generation sfermions are identical (first- and second-
 420 generation universality)

421 The introduction of such parameters, summarised in Table 1.3, defines the so-called
 422 **Phenomenological MSSM (pMSSM)**.

Table 1.3: Parameters in the pMSSM.

Parameter	Description	N. of parameters
M_1, M_2, M_3	Bino, Wino and gluino masses	3
M_A	pseudoscalar Higgs boson mass	1
μ	higgsino mass	1
$m_{\tilde{q}}, m_{\tilde{u}_R}, m_{\tilde{d}_R},$ $m_{\tilde{Q}_L}, m_{\tilde{t}}, m_{\tilde{b}}$	first- and second-generation squark masses third generation squark masses	3 3
$m_{\tilde{l}}, m_{\tilde{e}_R}$ $m_{\tilde{L}}, m_{\tilde{\tau}_R}$	first- and second-generation slepton masses third-generation slepton masses	2 2
A_t, A_b, A_τ	third-generation trilinear couplings	3
$\tan \beta$	two-higgs-doublet fields VEVs ratio	1

423 Such parameter space is still rather large and it makes **pMSSM** searches extremely chal-
 424 lenging and difficult to exclude. To overcome this problem *simplified models* are intro-
 425 duced. In other words, a certain signal process is extracted from the model and only

⁴²⁶ particles contributing to a certain decay mode will be considered, e. g. $\tilde{t}_1 \rightarrow t + \tilde{\chi}_1^0$ only
⁴²⁷ targets the 2-body decay ignoring the remaining SUSY mass spectrum. The number of
⁴²⁸ parameters will then boil down to 2; $m_{\tilde{t}}$ and $m_{\tilde{\chi}_1^0}$, allowing the reinterpretation of the
⁴²⁹ results and providing a powerful tool to constrain various models.

⁴³⁰ In this work only analyses based on such simplified models will be presented.

⁴³¹ Phenomenology of the top squark

⁴³² Fig. 1.6 shows SUSY particles production cross-sections in pp collisions at $\sqrt{s} = 13$ TeV for
⁴³³ squarks that do not contribute to gluino production diagrams and vice versa, i. e. treat-
⁴³⁴ ing squarks and gluinos as *decoupled* making the cross-section of squark pair-production
⁴³⁵ be the same for all families. While gluino pair-production cross-sections are fairly large,
⁴³⁶ SUSY electroweak production cross-sections of neutralinos and charginos are consider-
⁴³⁷ ably lower. Slepton production cross-section, which is not displayed, would sit just below
⁴³⁸ higgsino-like chargino/neutralino production cross-section.

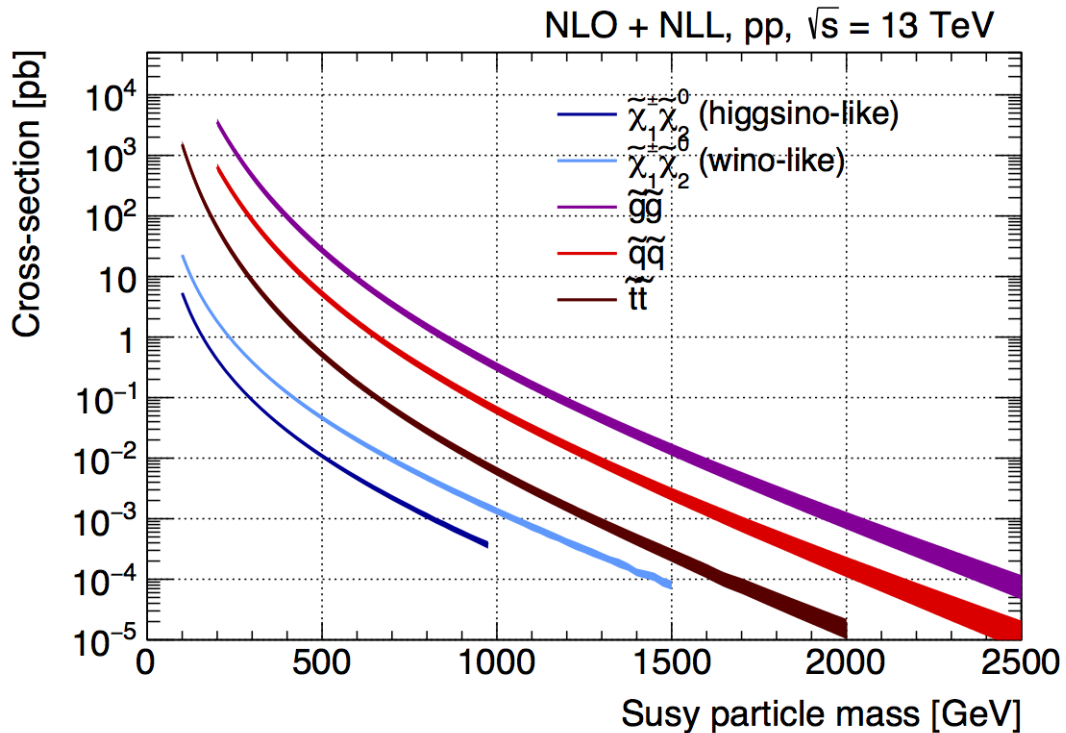


Figure 1.6: NLO+NLL production cross-sections as a function of mass at $\sqrt{s} = 13$ TeV [28]

⁴³⁹ There exists various decay modes of pair-produced stops, depending on the masses
⁴⁴⁰ of the decay products;

- ⁴⁴¹ • $\tilde{t} \rightarrow t \tilde{\chi}_1^0$
- ⁴⁴² • $\tilde{t} \rightarrow b \tilde{\chi}_1^\pm \rightarrow b W \tilde{\chi}_1^0$ (on/off-shell W) or $\tilde{t} \rightarrow b W \tilde{\chi}_1^0$ (off-shell top)
- ⁴⁴³ • $\tilde{t} \rightarrow c \tilde{\chi}_1^0$

- 444 • $\tilde{t} \rightarrow b f f' \tilde{\chi}_1^0$

445 Figure 1.7 shows a schematic representation of the parameter space $(m_{\tilde{t}_1}, m_{\tilde{\chi}_1^0})$ and
446 the different region where each of the above-mentioned process dominates.

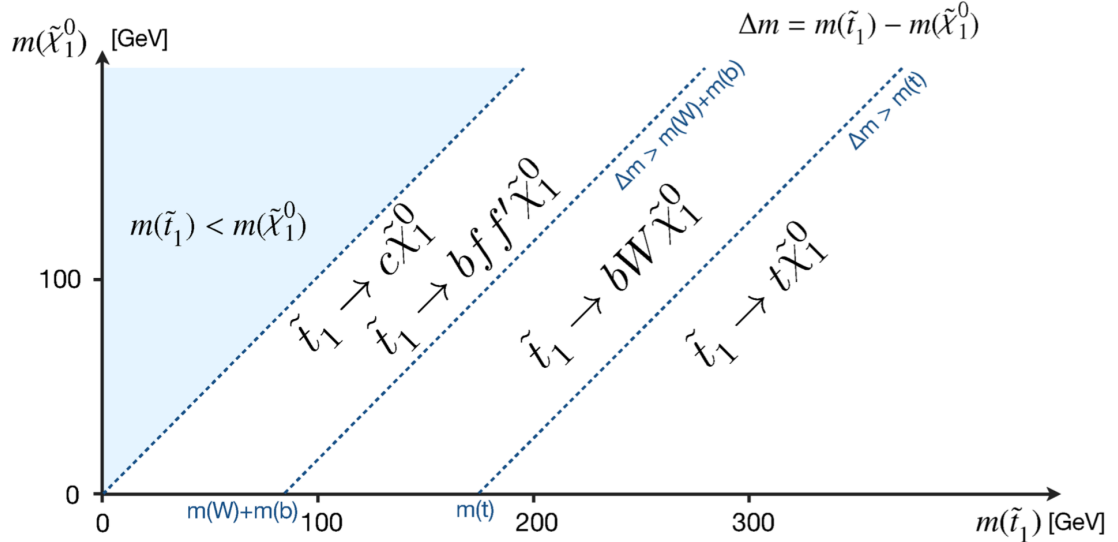


Figure 1.7: Illustration of stop decay modes in the $(m_{\tilde{t}_1}, m_{\tilde{\chi}_1^0})$ mass place where the $\tilde{\chi}_1^0$ is assumed to be the lightest supersymmetric particle. The dashed blue lines indicate thresholds separating regions where different processes dominate.

447 In the models considered in this work, either $\tilde{\chi}_2^0$ or $\tilde{\chi}_1^\pm$ is assumed to be the so-called
448 Next Lightest Supersymmetric Particle (NLSP). Three different decay scenarios were
449 considered in this work; (a) where both top squarks decay via $\tilde{t} \rightarrow t^{(*)} \tilde{\chi}_1^0$ ⁵; (b) at least
450 one of the stops decays via $\tilde{t} \rightarrow b \tilde{\chi}_1^\pm \rightarrow b W^{(*)} \tilde{\chi}_1^0$; (c) where $m_{\tilde{\chi}_2^0}$ is small enough to
451 allow one stop to decay via $\tilde{t} \rightarrow t \tilde{\chi}_2^0 \rightarrow h/Z \tilde{\chi}_1^0$. Here, h is the SM Higgs boson (125
452 GeV), as illustrated in Figure 1.8(a)–(c), respectively. Furthermore, top squarks can also
453 be indirectly produced through the so-called gluino-mediated stop production, as shown
454 in Figure 1.8(d).

455 Third-generation SUSY analyses, e. g. stop pair-production ($t\tilde{t}$) or sbottom pair-production
456 ($b\tilde{b}$) are very challenging, due to the cross-section being around a factor of six smaller
457 than $t\bar{t}$ production (when $m_{\tilde{t}_1} \sim m_t$), which usually is one of the main backgrounds. Fur-
458 thermore, the cross-section of such processes dramatically decreases with increasing $m_{\tilde{q}}$.
459 Nonetheless, for example, searches for direct \tilde{t}_1 production with $\tilde{t}_1 \rightarrow t + \tilde{\chi}_1^0$ are sensitive
460 in a scenario where $m_{\tilde{t}_1} \gg m_t + m_{\tilde{\chi}_1^0}$ as the large E_T^{miss} , from the neutralinos, provides
461 discriminating power for $t\bar{t}$ rejection.

⁵ The symbol (*) indicates the off-shell production

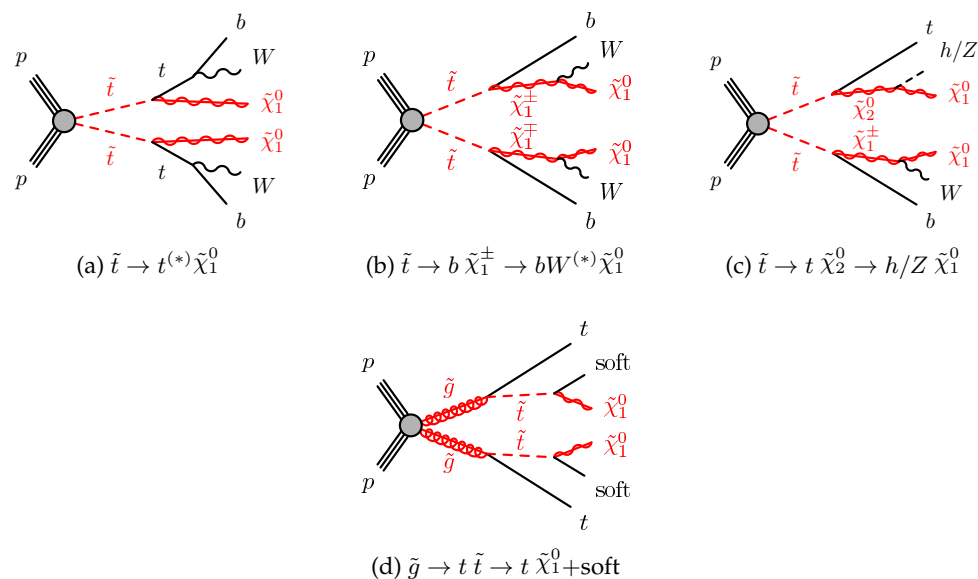


Figure 1.8: Diagrams of the decay topologies of the signal models considered in this work. The term “soft” refers to decay products that have transverse momenta below the detector thresholds.

462 **2 | The ATLAS Experiment**

463 **at the LHC**

464

*We are rather like children, who
must take a watch to pieces to see
how it works.*

Sir Ernest Rutherford

465 A Toroidal LHC ApparatuS ([ATLAS](#)) is one of the four main experiments¹ taking data
 466 at a center-of-mass energy of 13 TeV using beams delivered by the [LHC](#). In this chapter
 467 an overview of the [LHC](#) will be given in Section 2.1, then the [ATLAS](#) detector will be
 468 described in Section 2.2, and finally the Trigger system, used to cleverly select the data,
 469 will be described in Section 2.3. A more in-depth description of the Trigger algorithms I
 470 have been involved in will be given in Chapter 3.

471 **2.1 The LHC**

472 As of today, the [LHC](#) [29] is the world's largest and most powerful particle accelerator. It
 473 was designed to help answer some of the fundamental open questions in particle physics
 474 by colliding protons at an unprecedented energy and luminosity. It is located at [CERN](#),
 475 in the Geneva area, at a depth ranging from 50 to 175 metres underground. It consists
 476 of a 27-kilometre ring made of superconducting magnets, and inside it two high-energy
 477 particle beams travel in opposite directions and in separate beam pipes.

478 The beams are guided around the ring by a strong magnetic field generated by coils
 479 - made of special electric cables - that can operate in a superconducting regime. A total
 480 of 1232 superconducting dipole and 392 quadrupole magnets, with an average magnetic
 481 field of 8.3 T, are employed and kept at a temperature below 1.7 K, in order to preserve
 482 their superconducting properties. The formers are used to bend the beams and the latters
 483 to keep them focused while they get accelerated.

484 The collider first went live on September 2008 even though, due to a magnet quench

¹ [ATLAS](#), Compact Muon Solenoid ([CMS](#)), A Large Ion Collider Experiment ([ALICE](#)), Large Hadron Collider Beauty ([LHCb](#))

485 incident that damaged over 50 superconducting magnets, it has been operational since
 486 November 2009 when low-energy beams circulated in the tunnel for the first time since
 487 the incident. This also marked the start of the main research programme and the begin-
 488 ning of the so-called Run 1: first operational run (2009 - 2013).

489 Performance of the LHC

490 In June 2015 the **LHC** restarted delivering physics data, after a two-year upgrade pro-
 491 gramme, the so-called Long Shutdown 1 (**LS1**), during which the magnets were upgraded
 492 to handle the current required to circulate 7-TeV beams. It was the beginning of the so-
 493 called Run 2 - second operational run (2015-2018) - during which the **LHC** has collided
 494 up to 10^{11} bunches of protons every 25 ns at the design luminosity² of $2 \cdot 10^{34} \text{ cm}^{-2} \text{s}^{-1}$.
 495 The definiton of the luminosity is:

$$\mathcal{L} = f \frac{n_b N_1 N_2}{4\pi\sigma_x\sigma_y} \quad (2.1)$$

496 where N_1 and N_2 are the number of protons per bunch in each of the colliding beams, f
 497 is the revolution frequency of the bunch collisions, n_b the number of proton per bunch,
 498 and σ_x and σ_y are the horizontal and vertical dimensions of the beam. The luminosity is
 499 strictly related to the number of collisions occurring during a certain experiment via the
 500 following:

$$\mathcal{N}_{\text{event}} = \mathcal{L}\sigma_{\text{event}} \quad (2.2)$$

501 where σ_{event} is the cross section of the process under investigation. It has not only collided
 502 protons but also heavy ions, in particular lead nuclei at $\sqrt{s_{NN}} = 5.02 \text{ TeV}$, at a luminosity
 503 of $10^{27} \text{ cm}^{-2} \text{s}^{-1}$ [30].

504 Acceleration stages

505 Before reaching the maximum energy, the proton beams are accelerated by smaller ac-
 506 celerators through various stages. Figure 2.1 shows a sketch of the **CERN**'s accelerator
 507 complex. It all begins with the Linear Accelerator 2 (**LINAC2**). Here protons are acceler-
 508 ated up to 50 MeV, and then injected in the Proton Synchrotron Booster (**PSB**) where they
 509 reach 1.4 GeV. The next stage is the Parton Shower (**PS**), which boosts the beams up to 25
 510 GeV and then Super Proton Synchrotron (**SPS**) makes them reach energies up to 450 GeV.
 511 Eventually, the beams are injected in bunches with a 25 ns spacing into the **LHC**, where
 512 they travel in opposite directions, while they are accelerated to up to a center-of-mass
 513 energy of 13 TeV. Once the bunches reach the maximum energy, they are made collide at
 514 four different points, inside four experiments around the ring [29].

² the highest luminosity the detector was designed to cope with

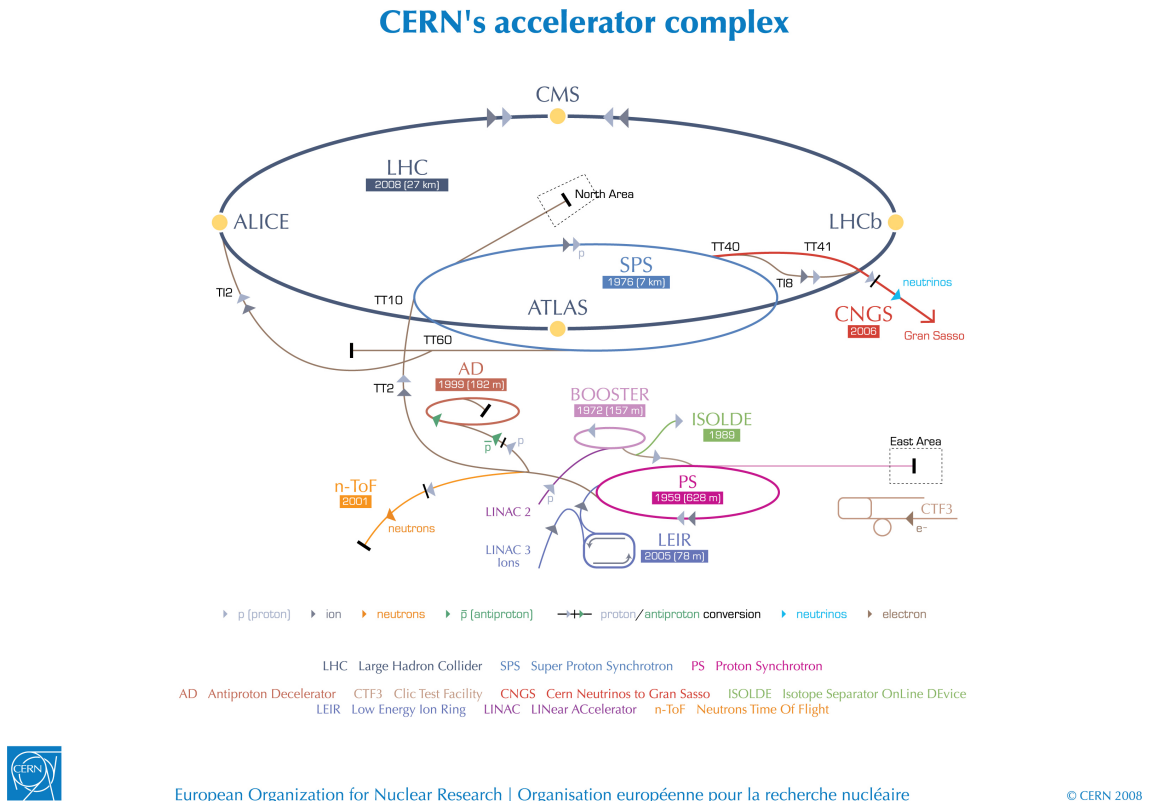


Figure 2.1: CERN Accelerator complex. The LHC is the last ring (dark grey line). Smaller machines are used for early-stage acceleration and also to provide beams for other experiments [31].

515 The heavy ion beams acceleration procedure is slightly different. Their journey starts
 516 at Linear Accelerator 3 (LINAC3), and the Low Energy Ion Ring (LEIR) then, before they
 517 make their way into the PS where they follow the same path as the protons.

518 The four large detectors on the collision points are; the multi-purpose detectors ATLAS [32],
 519 and CMS [33], LHCb [34], which focuses on flavour physics, and ALICE [35] which spe-
 520 cialises in heavy ion physics. The *big four* are not the only experiments at the CERN's ac-
 521 celerator complex. There also are smaller experiments based at the the four caverns about
 522 the collision points e.g. TOTal cross section, Elastic scattering and diffraction dissociation
 523 Measurement at the LHC (TOTEM) [36], Large Hadron Collider forward (LHCf) [37] and
 524 Monopole & Exotics Detector At the LHC (MoEDAL) [38], but these will not be discussed
 525 any further.

526 2.2 The ATLAS Detector

527 ATLAS is a general-purpose detector designed to collect data with the highest luminos-
 528 ity provided by the LHC. It is located at CERN's Point 1 cavern and it measures about
 529 45 m in length and 25 m in diameter. It has a forward-backward symmetric cylindrical
 530 geometry with respect to the interaction point and it is designed to reconstruct and mea-
 531 sure physics objects such as electrons, muons, photons and hadronic jets. Its design was
 532 optimised to be as sensitive as possitble to the discovery of the Higgs boson and Beyond

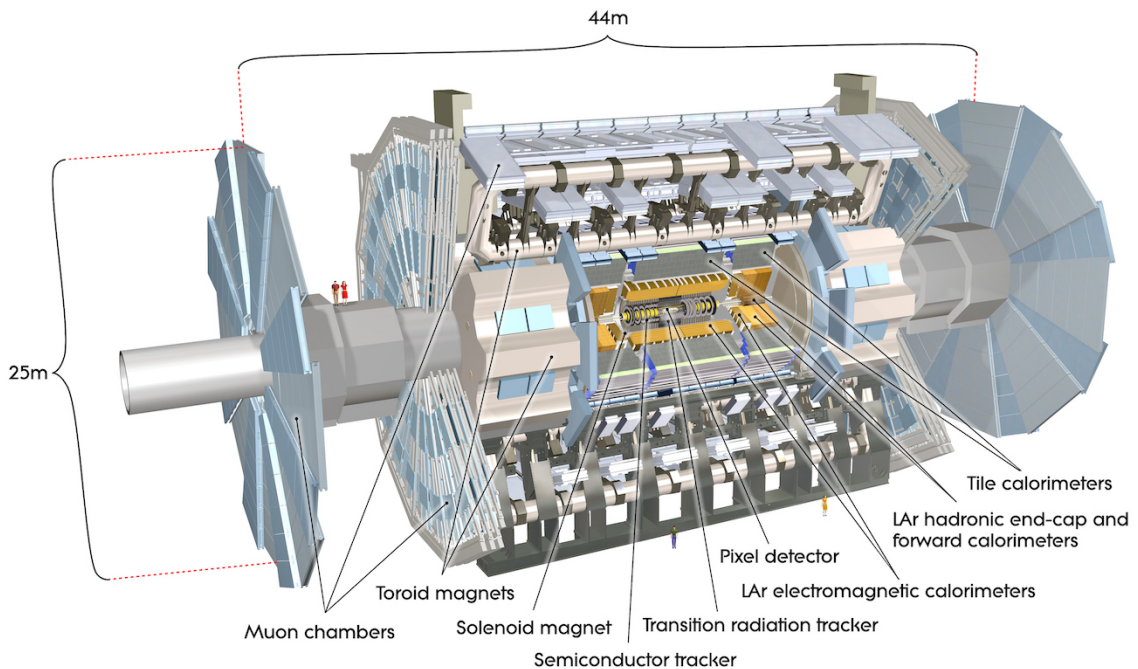


Figure 2.2: Cut-away view of the [ATLAS](#) detector. The dimensions of the detector are 25 m in height and 44 m in length. The overall weight of the detector is approximately 7000 tonnes [31].

533 Standard Model ([BSM](#)) physics. In fact, thanks to its various sub-systems, [ATLAS](#) is able
 534 to observe all possible decay products by covering nearly 4π steradians of solid angle.

535 In Figure 2.2 a cut-away view of [ATLAS](#) with all its components is shown. The inner-
 536 most layer is the Inner Detector ([ID](#)) which is the core of the tracking system and consists
 537 of a Pixel, a SemiConductor Tracker ([SCT](#)), and a Transition Radiation Tracker ([TRT](#)). It is
 538 submerged in a 2 T magnetic field, generated by a thin superconducting solenoid, which
 539 bends all the charged particles' trajectories allowing transverse momentum measure-
 540 ment. The electromagnetic and hadronic calorimeters form the next layer and they are
 541 both used to perform precise energy measurements of photons, electrons, and hadronic
 542 jets. Finally, the outermost layer corresponds to the Muon Spectrometer ([MS](#)), enclosed
 543 in a toroidal magnetic field, which, together with the [ID](#), allows precise measurement of
 544 momentum and position of muons. These sub-detectors will be discussed in more detail
 545 in the following sections.

546 The ATLAS coordinate system

547 A coordinate system is taken on for the spatial definition of the sub-systems and kin-
 548 ematic measurement of physics processes. Such system is defined starting from the in-
 549 teraction point, defined as the origin. The z -axis is defined by the beam direction and the
 550 $x - y$ plan, as transverse to the beam direction.

551 A quantity, known as pseudorapidity, (η), is defined to describe the angle of a particle
 552 coming out of the collision, with respect to the beam axis:

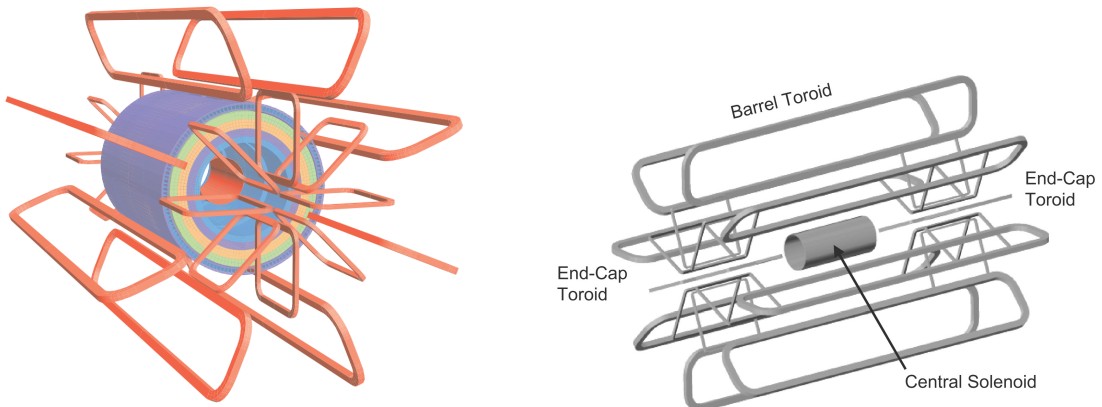
$$\eta \equiv -\ln(\tan(\theta/2))$$

553 Here θ is the polar angle. The azimuthal angle, ϕ , is defined around the beam axis and
 554 the polar angle. In the (η, ϕ) space a distance ΔR can be therefore defined as

$$\Delta R = \sqrt{\Delta\eta^2 + \Delta\phi^2}$$

555 where $\Delta\eta$ and $\Delta\phi$ are the differences in pseudorapidity and azimuthal angle between
 556 any two considered objects. A central and a forward region of pseudorapidity are also
 557 defined such that the detector components are described as part of the *barrel* if they belong
 558 to the former or as part of the *end-caps* if they belong to the latter.

559 2.2.1 The Magnet System



(a) Geometry of magnet windings and tile calorimeter steel. The eight barrel toroid coils, with the end-cap coils interleaved are visible. The solenoid winding lies inside the calorimeter volume [32].

(b) Schematic view of the superconducting magnets [39].

Figure 2.3: The [ATLAS](#) magnet system.

560 The [ATLAS](#) magnet system, 26 m long with a 22 m diameter, generates the magnetic
 561 field needed to bend the trajectories of charged particles in order to perform momentum
 562 measurement. Figure 2.3a and 2.3b show the geometry of the system and its compo-
 563 nents, which are made of NbTi - superconducting material - and will be described in the
 564 following paragraphs.

565 The Central Solenoid

566 With an axial length of 5.8 m, an inner radius of 2.46 m, and an outer radius of 2.56 m, the
 567 central solenoid magnet is located between the [ID](#) and the Electronic Calorimeter ([ECAL](#)).
 568 Its function is to bend the charged particles that go through the [ID](#) and it is aligned on

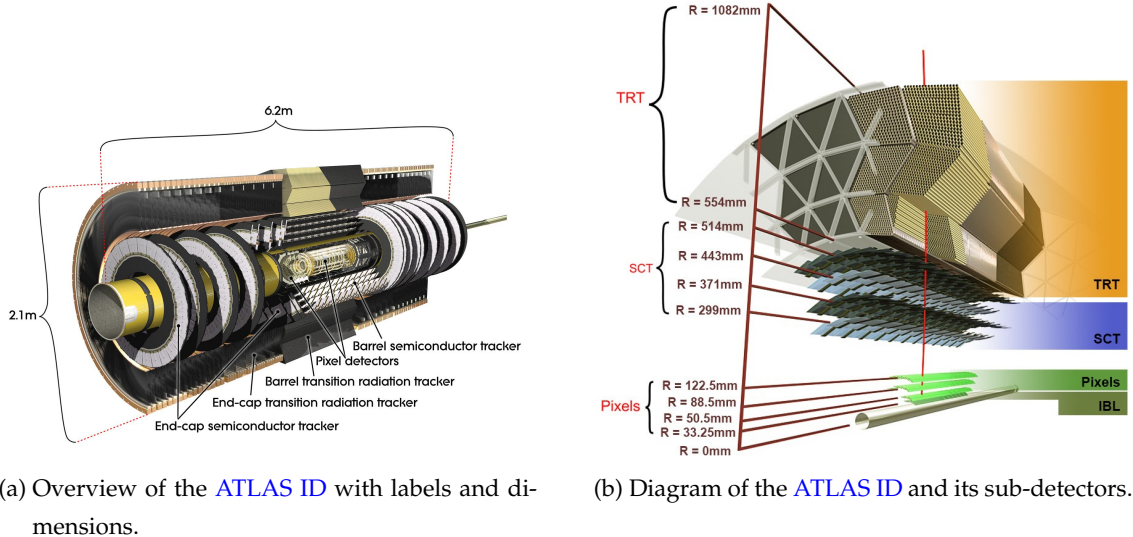
the beam axis providing a 2 T axial magnetic field that allows accurate momentum measurement up to 100 GeV [39].

571 The Barrel and the End-cap Toroids

572 Figure 2.3b displays the toroid magnetic system that surrounds the calorimeters. With
 573 its cylindrical shape this component consists of a barrel and two end-caps toroids. The
 574 barrel toroid is comprised of eight coils and produces an approximately 0.5 T toroidal
 575 magnetic field for the central muon detectors. The end-cap toroids, also comprised of
 576 eight coils each, produce an approximately 1 T toroidal magnetic field, which is required
 577 to provide bending power for the end-cap regions of the muon spectrometer.

578 2.2.2 The Inner Detector

579 The ID [40] is the innermost component of the ATLAS detector i.e. the nearest sub-
 580 detector to the interaction region and it is used to reconstruct charged particle tracks
 581 used in the selection of physics objects. In fact, it allows robust track reconstruction,
 582 with accurate impact parameter resolution ($\sim 20\mu m$) and precise primary and secondary
 583 vertex reconstruction for charged particles (tracks) above 500 MeV and within $|\eta| < 2.5$.



(a) Overview of the ATLAS ID with labels and dimensions.

(b) Diagram of the ATLAS ID and its sub-detectors.

Figure 2.4: The ATLAS Inner Detector

584 The ID is comprised of independent and concentric sub-systems, which are all shown
 585 in Figure 2.4:

- 586 • Insertable B-Layer (IBL):

587 innermost Pixel Detector layer added during ATLAS Run 2 upgrade (2013/2014)
 588 to improve vertexing, by a factor ~ 1.4 , and impact parameter reconstruction, by a
 589 factor 2;

- 590 • Silicon Pixel Tracker (Pixel):
591 made of silicon pixel layers and used mainly for reconstructing both the primary
592 and secondary vertices in an event;
- 593 • SCT:
594 comprised of silicon microstrip layers; thanks to its resolution ($17 \times 580 \mu\text{m}$) it can
595 accurately measure particle momenta;
- 596 • TRT:
597 final layer comprised of various layers of gaseous straw tube elements surrounded
598 by transition radiation material.

599 These sub-detectors will be discussed in the following sections.

600 **IBL**

601 The IBL [41] is the innermost Pixel Detector layer as shown in Figure 2.4b. It is com-
602 prised of 6M channels and each pixel measures $50 \times 250 \mu\text{m}$. Its resolution is $8 \times 40 \mu\text{m}$.
603 The addition of this new layer produced an improvement on the quality of the impact
604 parameter reconstruction of tracks almost by a factor 2, and almost by a factor 1.4 on the
605 resolution of the reconstructed primary vertex, highly important e. g. for the tagging of
606 bottom-quark-initiated jets (b -jets).

607 **Pixel**

608 The Pixel detector is comprised of 1750 identical sensorchip-hybrid modules, each cover-
609 ing an active area of $16.4 \times 60.8 \text{ mm}$. The total number of modules correspond to roughly
610 80 million semiconductor silicon pixels. The nominal pixel size is $50 \mu\text{m}$ in the ϕ direction
611 and $400 \mu\text{m}$ in the barrel region, along the z -axis (beam axis) [42]. The reason why such a
612 large amount of pixels is employed is justified by the need to cope with the high luminos-
613 ity in ATLAS. The silicon pixel detector measures 48.4 cm in diameter and 6.2 m in length
614 providing a pseudorapidity coverage of $|\eta| < 2.5$. Figure 2.4b shows the three concentric
615 barrel layers placed at 50.5 mm, 88.5 mm and 122.5 mm respectively. Furthermore, the
616 Pixel detector is made of six disk layers, three for each forward region, such that when a
617 charged particle crosses the layers it will generate a signal at least in three space points.
618 The fine granularity of such detector allows accurate measurement and precise vertex
619 reconstruction, as it provides a more accurate position measurement as a large detection
620 area is available. In particular, it has a resolution of $10 \times 115 \mu\text{m}$.

621 **SCT**

622 The SCT is made of 4088 modules of silicon micro-strip detectors arranged in four con-
623 centric barrel layers. It is mainly used for precise momentum reconstruction over a range

624 $|\eta| < 2.5$ and it was designed for precision measurement of the position using four points
 625 (corresponding to eight silicon layers), obtained as track hits when crossing the layers.
 626 Figure 2.4b shows the structure of the **SCT** with its four concentric barrel layers with
 627 radii ranging from 299 mm to 514 mm and two end-cap layers. Each module has an
 628 intrinsic resolution of $17 \mu\text{m}$ in the $R - \phi$ direction and $580 \mu\text{m}$ in the z direction. As
 629 the **SCT** is further away from the beam-pipe than the Pixel detector, it has to cope with
 630 reduced particle density. This allows for reduced granularity maintaining the same level
 631 of performance of the Pixel detector: **SCT** can use ~ 6.3 million read-out channels.

632 **TRT**

633 The last and outermost of the sub-systems in the **ID** is the **TRT**. It is a gaseous detector
 634 which consists of 4 mm diameter straw tubes wound from a multilayer film reinforced
 635 with carbon fibers and containing a $30 \mu\text{m}$ gold plated tungsten wire in the center. The
 636 straw is filled with a gas mixture of 70% Xe, 27% CO₂ and 3% O₂ [43]. As shown in Fig-
 637 ure 2.4b, its section consists of three concentric layers with radii ranging from 554 mm to
 638 1082 mm, each of which has 32 modules containing approximately 50,000 straws, 1.44 m
 639 in length, aligned parallel to the beam direction with independent read-out at both ends.
 640 The gas is ionised when a charged particle passes through it and electrons (ions) are col-
 641 lected at the anode (cathode). A current in the wire will be created and as the electric
 642 field in the tube is known, the distance from the wire can be calculated using the time
 643 that electrons take to drift to the wire. Furthermore, the **TRT** is capable of performing
 644 particle identification on the particles that pass through it by utilising the detection of
 645 transition radiation photons that are emitted when a highly relativistic charged particle
 646 crosses a boundary between two media with different dielectric constants. The separ-
 647 ation between, e.g. electrons and charged pions is achieved by observing the amount
 648 of transition radiation produced, since this is dependent on how relativistic the charged
 649 particle is.

650 The **TRT** has an intrinsic resolution of $130 \mu\text{m}$ and, on average, 35 hits are observed
 651 within such sub-system when a charged particle passes through.

652 **Performance of the ID**

653 As previously mentioned, the tracking performed by the **ID** is indispensable to measure
 654 the properties of objects such as leptons and jets, as well as interaction vertices in a cer-
 655 tain event and secondary vertices, which are used e.g. to identify bottom-quark-initiated
 656 jets(*b*-jets). Both jets and *b*-jets are expected in the final states that are being searched for
 657 in this thesis.

658 The overall performance of the **ID** depends on the three sub-systems and it can be

659 shown in terms of momentum resolution:

$$\frac{\sigma_{p_T}}{p_T} = 1.6 \pm 0.1\% \oplus \frac{(53 \pm 2) \times 10^{-5}}{\text{GeV}} \times p_T \quad (2.3)$$

660 measured in [44] using cosmic muons before the addition of the **IBL**. Eq. 2.3 shows that
 661 the **ID** has a momentum resolution of $\sim 1.6\%$ at low momenta ($\sim 1 \text{ GeV}$) and of $\sim 50\%$
 662 at 1 TeV .

663 2.2.3 The Calorimeters

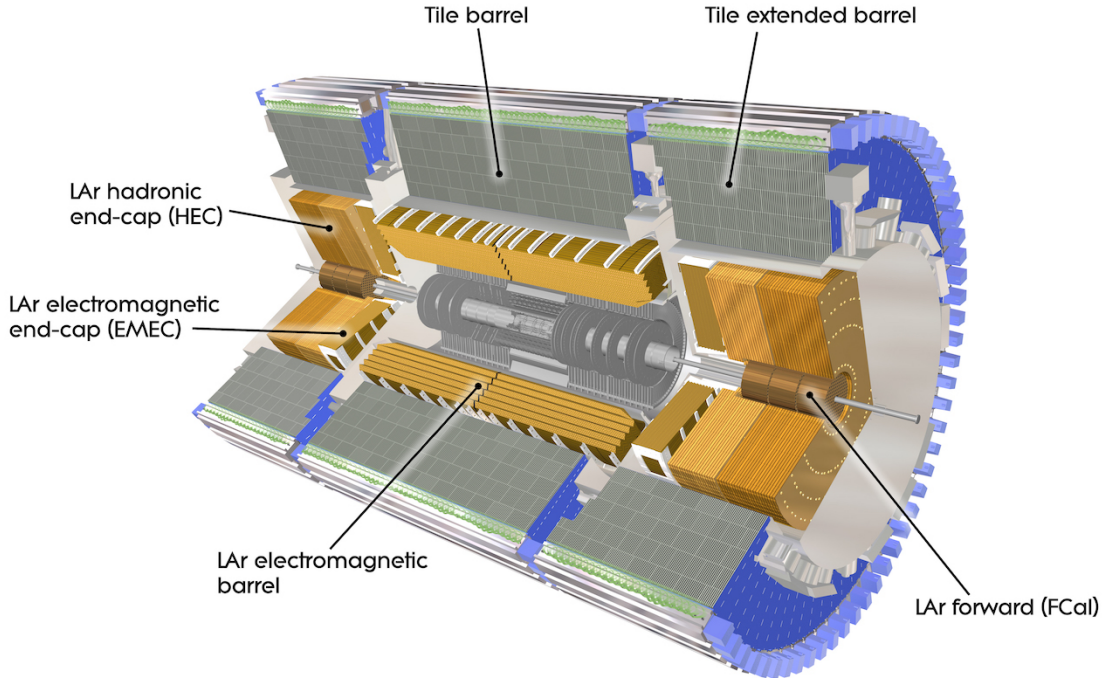


Figure 2.5: A computer generated image of the full calorimeter.

664 The **ATLAS** Calorimeter system, shown in Figure 2.5, is comprised of two main sub-
 665 systems; the **ECAL** and Hadronic Calorimeter (**HCAL**), which are designed to stop and
 666 measure the energy of electromagnetic-interacting and hadronic particles respectively.
 667 The combination of the two provides full coverage in ϕ and $|\eta| < 4.95$. Particles slow
 668 down and lose energy generating showers when crossing different layers. The **ECAL** is
 669 comprised of one barrel and two end-cap sectors employing Liquid Argon (**LAr**). The
 670 showers hereby develop as electrons pairs which are then collected. The **HCAL** is also
 671 comprised of one barrel and two end-cap sectors. The sensors in the barrel of the **HCAL**
 672 are tiles of scintillating plastic whereas **LAr** is employed for the end-cap. A forward
 673 region, the closest possible to the beam, is covered by a **LAr** forward calorimeter (**FCal**).
 674 The **LAr** and Tile Calorimeter will be briefly discussed in the following paragraphs.

675 The Liquid Argon Calorimeter

676 The **ECAL** is comprised of multiple layers of **LAr** sampler and lead absorber. The choice
 677 of its accordion-geometry design brought two main advantages; full ϕ coverage with no
 678 non-interactive regions (no cracks); fast extraction of signals coming from both front or
 679 rear end of the electrodes. It is made of two half-barrel wheels, both placed in the bar-
 680 rel cryostat, that provide a pseudorapidity coverage up to $|\eta| < 1.475$ and two end-cap
 681 detectors providing $1.375 \leq |\eta| \leq 3.20$ coverage in two end-cap cryostats. The junc-
 682 tion between the barrel and end cap components defines the crack region and any signal
 683 coming from the crack region is therefore discarded.

684 In the $|\eta| < 1.8$ region there is an additional layer, placed at the front of the calori-
 685 meter, that is made of a thin (0.5 cm in the end-cap and 1.1 cm in the barrel) **LAr** layer
 686 with no absorber [45]. This additional layer was designed to correct for the energy lost,
 687 as particles enter the calorimeter, by taking a measurement just before the majority of the
 688 electromagnetic shower is developed.

689 The Tile calorimeter

690 The main purpose of the hadronic calorimeter is to measure the energy of hadronic
 691 showers. It is built employing steel and scintillating tiles coupled to optical fibres which
 692 are read out by photo-multipliers. As shown in Figure 2.5, the **HCAL** is made up of three
 693 cylinders; a central barrel, 5.64 m long covering a region $|\eta| < 1.0$, and two extended
 694 barrel, 2.91 m long covering a region $0.8 < |\eta| < 1.7$. Each cylinder is made up of 64
 695 modules and each module is in turn made up of three layers. Ultimately, the smallest
 696 section of the calorimeter module is a cell with a $\Delta\phi \times \Delta\eta = 0.1 \times 0.1$ granularity for the
 697 two innermost layers and $\Delta\phi \times \Delta\eta = 0.2 \times 0.1$ for the outermost one.

698 Performance of the Calorimeter

699 The performance of the calorimeter is important to measure the properties of the jets
 700 used in the analyses presented in this thesis. This has been assessed using test beam data
 701 and, once the noise has been subtracted from the experimental measurements these are
 702 fit using Eq. 2.4

$$\frac{\sigma(E)}{E} = \frac{a}{\sqrt{E[\text{GeV}]}} \oplus b \quad (2.4)$$

703 Here, a is the stochastic term and b is a constant that includes local non-uniformities in
 704 the calorimeter response.

705 The **ECAL** performance in the barrel was assessed firing an electron beam at a module
 706 that is identical to those in **ATLAS** and the fitted energy resolution is $\sigma(E)/E = (10 \pm$
 707 $0.4)\%/\sqrt{E} \oplus (0.4 \pm 0.1)\%$ with a variation of no more than 0.7% for the entire coverage of
 708 the calorimeter.

709 The **HCAL** performance in the barrel was assessed firing a pion beam at a prototype
 710 detectors of the **LAr** electromagnetic and tile calorimeters. The fitted energy resolution
 711 (with an added term to account for electronic noise) is $\sigma(E)/E = (52 \pm 1.0)\%/\sqrt{E} \oplus (3.0 \pm$
 712 $0.1)\% \oplus (1.6 \pm 0.1)/E$.

713 2.2.4 The Muon Spectrometer

714 The **MS** [46], shown in Figure 2.6, is the outermost sub-system of the whole **ATLAS** de-
 715 tector. As such, it surrounds the calorimeters and its main function is to perform precision
 716 measurement of muons momenta. The deflection of muon tracks employing large super-
 717 conducting air-core toroid magnets and high-precision tracking chambers is at the heart
 718 of such high precision measurement.

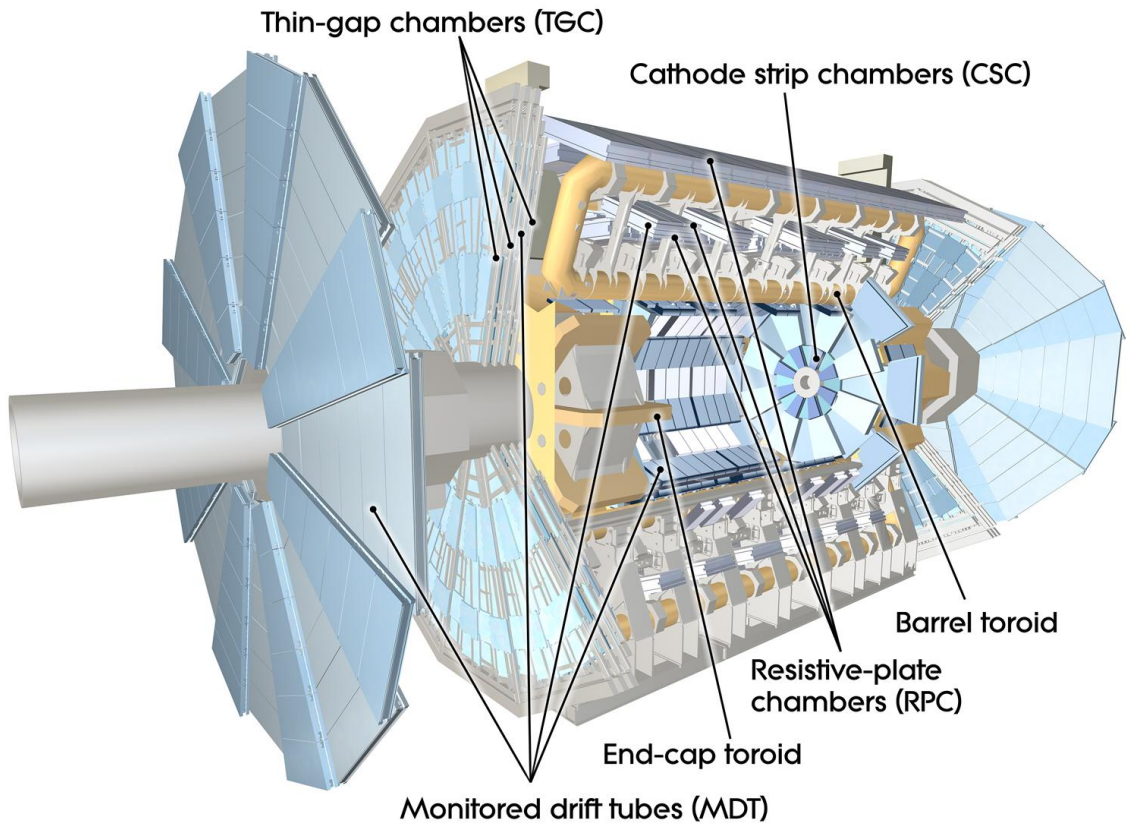


Figure 2.6: Cut-away view of the **ATLAS** muon system [32].

719 The **MS** is comprised of one large barrel toroid, covering the region $|\eta| \leq 1.4$, and two
 720 end-cap toroids, covering $1.6 < |\eta| \leq 2.7$ which are employed together to achieve the
 721 track-bending effect wanted. The magnitude of the magnetic field in the barrel, generated
 722 by eight large superconducting coils, ranges from 0.5 to 2 T.

723 Around the beam axis, three cylindrical layers make way for the chambers, placed in
 724 planes perpendicular to the beam, used to measure tracks.

725 Monitored Drift Tubes (**MDTs**) are employed over most of the pseudorapidity range
 726 to provide precision measurement of track coordinates in the bending direction. An MDT

is essentially a set of 30-mm-diameter *Al* tubes containing a *W-Re* (Tungsten-Rhenium) wire, surrounded by a non-flammable Ar-CH₄-N₂ mixture at a pressure of 3 bar. The resolution a single wire can give on the particle position is 80 μm enhanced by having multiple layers of tubes for each module.

Cathode Strip Chambers ([CSCs](#)) are instead employed at large pseudorapidity ($2 < |\eta| < 2.7$). They work similarly to the MDT but instead of tubes there are cathode strips above and below the anode wires. In particular, one set is orthogonal to the wires for precision measurement and the other one parallel to the wires providing a measurement of the transverse coordinate. The gas employed between the strips and wires is a non-flammable mixture of Ar-CO₂-CF₂.

Thin-Gap Chambers ([TGCs](#)) are employed in the end-cap region and Resistive-Plate Chambers ([RPCs](#)) in the barrel. The [TGCs](#) are very similar to the [CSCs](#). They provide large signals and in a very narrow time window making them ideal for triggering purposes.

The [RPCs](#) are also gas-based detectors. They are comprised of two parallel resistive plates held apart by insulating spacers, and a uniform electric field is employed to generate a limited avalanche multiplication centred around the primary ionisation electron. This will then be detected by *Al* strips separated from the plates by an insulating film.

2.3 The ATLAS Trigger System

The [ATLAS](#) Trigger System is at the heart of data taking. It is an essential component of any nuclear or particle physics experiment as it is responsible for deciding whether or not to store an event for later study. Its main function to reduce the event rate from ~ 40 MHz bunch-crossing³ to ~ 1 kHz.

The Trigger system employs a two-level system: a first hardware-based trigger, Level-1 ([L1](#)) Trigger, and a software-based, High Level Trigger ([HLT](#)). [L1](#) processes low-granularity information from the calorimeter and the muon spectrometer and identifies the so-called Regions of Interest (RoIs)⁴ before making a decision. Event data from other sub-syststem are temporarily stored in memories whilst [L1](#) decision is taken.

Further investigations are left to [HLT](#) which is made of software running on a cluster of computers ([HLT](#) farm). Additionally, a Fast TracKer ([FTK](#)) system [47] (to be installed before the end of Run 2) will process events that are accepted by [L1](#) trigger, and seed the [HLT](#) algorithms. It will provide global ID track reconstruction at the [L1](#) trigger rate using lookup tables stored in custom associative memory chips for the pattern recognition.

The [ATLAS](#) trigger system will be further discussed in Chapter 3, however the Run-1-to-Run-2 upgrade of the [ATLAS](#) trigger will not be discussed any further.

³ The term bunch-crossing, $\langle \mu \rangle$, is hereby used when referring to a collision between two bunches of protons.

⁴ $\eta - \phi$ regions where event features have been found by the [L1](#) selection process.

762 3 | The ATLAS Trigger System

763

*Software is a great combination
between artistry and engineering.*

Bill Gates

764 The [ATLAS](#) trigger system together with its performance will be presented in this
 765 chapter. A brief introduction about the reason behind the need of a trigger system, to-
 766 gether with its implementation in [ATLAS](#), will be discussed in Section 3.1. The [L1](#) trigger
 767 and [HLT](#) will be discussed in Sections 3.2 and 3.3, respectively. Finally, Section 3.3.2
 768 will be dedicated to the performance of [HLT](#) for low- p_T single-lepton, and medium- and
 769 high- p_T b -jet triggers - which has been part of the *qualification task*¹ of the author -, to-
 770 gether with the performance of the missing transverse energy trigger, E_T^{miss} , - as the most
 771 relevant trigger for the analysis discussed in Chapter 5.

772 3.1 Overview

773 More than 80 fb^{-1} of pp collisions were delivered in 2016 and 2017 by the [LHC](#) and, due
 774 to storage space limitations, it is not feasible to save all the information about the collision
 775 after every bunch crossing, so the [ATLAS](#) Trigger System is indispensable to reduce the
 776 read-out rate to a sensible value without affecting the physics programme of [ATLAS](#),
 777 e.g. discarding potentially interesting events. A multiple-level architecture is employed
 778 to allow the trigger enough time to identify interesting events, using both software- and
 779 hardware-based real-time algorithms.

780 Figure 3.1 shows the Trigger and Data Quality ([TDAQ](#)) system. This is comprised of
 781 both a hardware-based first-level trigger ([L1](#)) and a software-based [HLT](#), as already men-
 782 tioned in Section 2.3. The [L1](#) trigger decision is formed by the Central Trigger Processor
 783 ([CTP](#)), which receives inputs from the L1 Calorimeter ([L1Calo](#)) and L1 Muon ([L1Muon](#))
 784 triggers. Once the events pass the [L1](#) selection, they are buffered in the Read-Out Sys-
 785 tem ([ROS](#)) and processed by the [HLT](#), which receives information on the Region of In-
 786 terest ([RoI](#)) from [L1](#) to be used for track reconstruction in the trigger algorithms. An [RoI](#)

¹ In order to become an [ATLAS](#) author, a person must have been an active [ATLAS](#) member for at least one year working on a technical work

is an extended wedge-shaped spatial region in the detector, consisting of a direction in $\eta - \phi$ originating from a z -position along the beamline, extended along the beamline by independent directions with respect to this z position, and extended about the ϕ direction with independent directions in pseudorapidity, at the maximum and minimum z positions along the beamline.

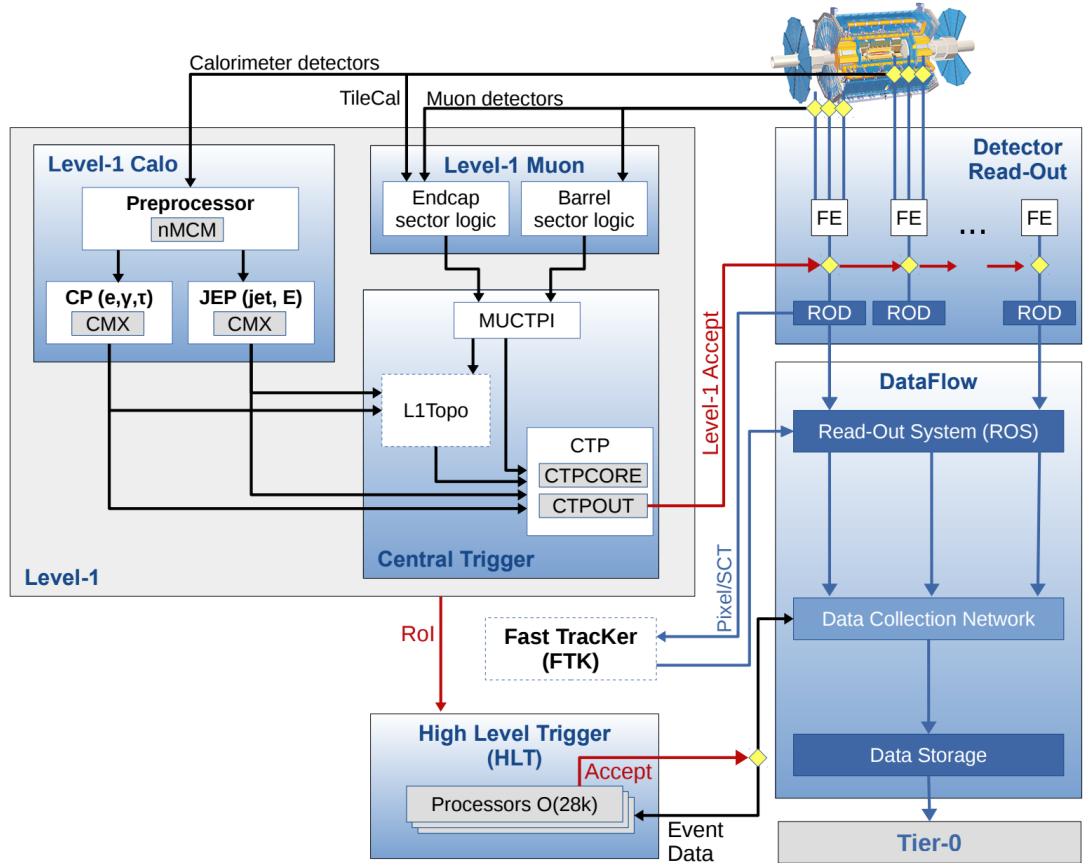


Figure 3.1: The [ATLAS TDAQ](#) system. [L1Topo](#) and [FTK](#) [48] have not been used for the results shown in this thesis.

The trigger system is configured via the so-called trigger *menu* which contains the multiplicity requirement (number of tracks) and the prescale factors². Additionally, the menu is meant to define the trigger *chains* - usually referred to just as trigger - that start from a [L1](#) trigger and specify a sequence of reconstruction and selection steps for the specific trigger signatures required in the trigger chain.

3.2 Level-1 Trigger

The [L1](#) trigger decision is essentially taken by the [CTP](#), based on the information the [L1](#) calorimeter and [L1](#) muon trigger systems. Additionally, a Level-1 Topological ([L1Topo](#))

² A factor associated with a trigger at each level that indicates what fraction of events, that could pass this trigger selection, is actually accepted.

800 trigger³, fed with energy and direction information about the objects found by the [L1Calo](#)
 801 and [L1Muon](#) triggers, is employed [32, 48, 49].

802 The [L1](#) trigger system is implemented in fast custom electronics to keep the decision
 803 time around $2.5\ \mu\text{s}$ and its decision is used as a *seed* for [HLT](#).

804 The L1 Calorimeter Trigger

805 The [L1Calo](#) trigger [32, 50] is based on inputs from the electromagnetic and hadronic
 806 calorimeters within the region $|\eta| < 4.9$. It provides triggers for objects such as elec-
 807 trons/photons, taus, jets, and global transverse energy. Dedicated analogue trigger sig-
 808 nals, provided by the [ATLAS](#) calorimeters independently from the signals read out and
 809 used at the [HLT](#) and offline, make the [L1Calo](#) trigger decision, which is based on the
 810 information from analogue sums of calorimeter elements, called *trigger towers*, instead of
 811 using the full granularity of the calorimeter. The trigger towers have a size of approxim-
 812 ately $\Delta\eta \times \Delta\phi = 0.1$ in the central part of the calorimeter, $|\eta| < 2.5$, and they get larger
 813 and less regular in the forward region. Separate trigger towers are employed for electro-
 814 magnetic and hadronic calorimeters. Furthermore, two processor systems run the trigger
 815 algorithms, once the signals have been digitised: the first, called *cluster processor*, uses the
 816 full [L1](#) trigger granularity information in the central region to look for small and local-
 817 ised clusters, which are typical a energy deposit left by an electron, photon or tau; the
 818 second, the *jet and energy-sum processor*, uses 2×2 sums of trigger towers (jet elements),
 819 to identify jet candidates and form missing transverse energy, $E_{\text{T}}^{\text{miss}}$, and total transverse
 820 energy, E_{T} . As an example, Figure 3.2 shows a sketch of the electron/photon and tau
 821 triggers. The trigger algorithm identifies a Region of Interest as a 2×2 trigger tower
 822 cluster in the electromagnetic calorimeter for which the transverse-energy sum, released
 823 in at least one of the four possible pairs of nearest neighbour towers (1×2 or 2×1), ex-
 824 ceeds a pre-defined threshold. Additionally, jets RoIs are defined as 4×4 , 6×6 or 8×8
 825 trigger-tower windows for which the summed electromagnetic and hadronic transverse
 826 energy exceeds pre-defined thresholds and which surround a 2×2 trigger tower core that
 827 is a local maximum that will be also used to define the coordinates of the jet [RoI](#).

828 The L1 Muon Trigger

829 The [L1Muon](#) trigger system [52] processes input data from fast muon trigger sub-detectors
 830 and its main task is to select muon candidates with a p_{T} threshold of 6 GeV and identify
 831 the bunch crossing in which they were produced.

832 Figure 3.3 shows how muons are triggered at [L1](#). The [RPC](#) system in the barrel region
 833 ($|\eta| < 1.05$) and the [TGC](#) system in the end-cap regions ($1.05 < |\eta| < 2.4$) are employed.
 834 They provide a rough measurements of muon-candidate p_{T} , η , and ϕ . Three planes in the
 835 barrel and three in each endcap form the trigger chambers. Each plane is comprised of

³ Two FPGA-based (Field-Programmable Gate Arrays) processor modules

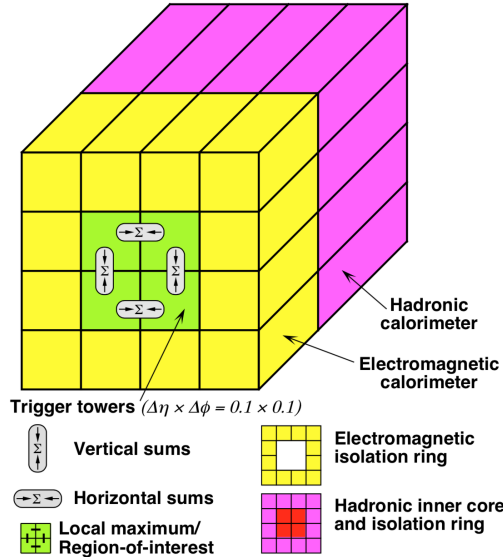


Figure 3.2: Illustration of the electron/photon and tau algorithms with the sums to be compared to programmable thresholds (from [51]).

836 two to four layers and muon candidates are identified by forming coincidences between
 837 the muon planes. Coincidences are formed requiring hits that lie within parametrised
 838 geometrical muon *roads*. A road, as the example shown in Figure 3.3, essentially con-
 839 tains the trajectories, from the interaction point, of either positively or negatively charged
 840 muons with a p_T above a given threshold. In particular six programmable p_T thresholds
 841 are employed at L1, divided into two sets: three low- p_T thresholds meant to cover values
 842 up to 10 GeV, and three high- p_T thresholds meant to cover $p_T > 10$ GeV.

843 The CTP

844 The **CTP** [32] applies the multiplicity requirements and prescale factors specified in the
 845 trigger menu to the inputs from the **L1** trigger systems and forms the **L1** trigger de-
 846 cision. Timing and control signals⁴ are employed to distribute the **L1** trigger decision to
 847 all **ATLAS** sub-detector readout systems. It is responsible for applying the so-called *pre-*
 848 *ventive dead-time*, meant to limit the minimum time between two consecutive **L1** accepts
 849 (*simple dead-time*), $\mathcal{O}(100\text{ns})$, in order to both avoid overlapping readout windows, and
 850 restrict the number of **L1** accepts allowed in a given number of bunch-crossings (*complex*
 851 *dead-time*) to avoid buffers from overflowing. In addition, a *busy dead-time*, can be intro-
 852 duced by **ATLAS** sub-detectors to temporarily throttle the trigger rate. These dead-times
 853 are used to monitor the total **L1** trigger rate, and individual trigger rates that need to be
 854 monitored before and after any prescales and/or any vetoes that have been applied. Fur-
 855 thermore, such information is also used to provide a measure of the **L1** dead-time, which
 856 has to be accounted for when determining the luminosity [51].

⁴ The timing signals are defined with respect to the **LHC** bunch crossings: a 25 ns time window centred on the instant at which a proton bunch might cross the **ATLAS** interaction point.

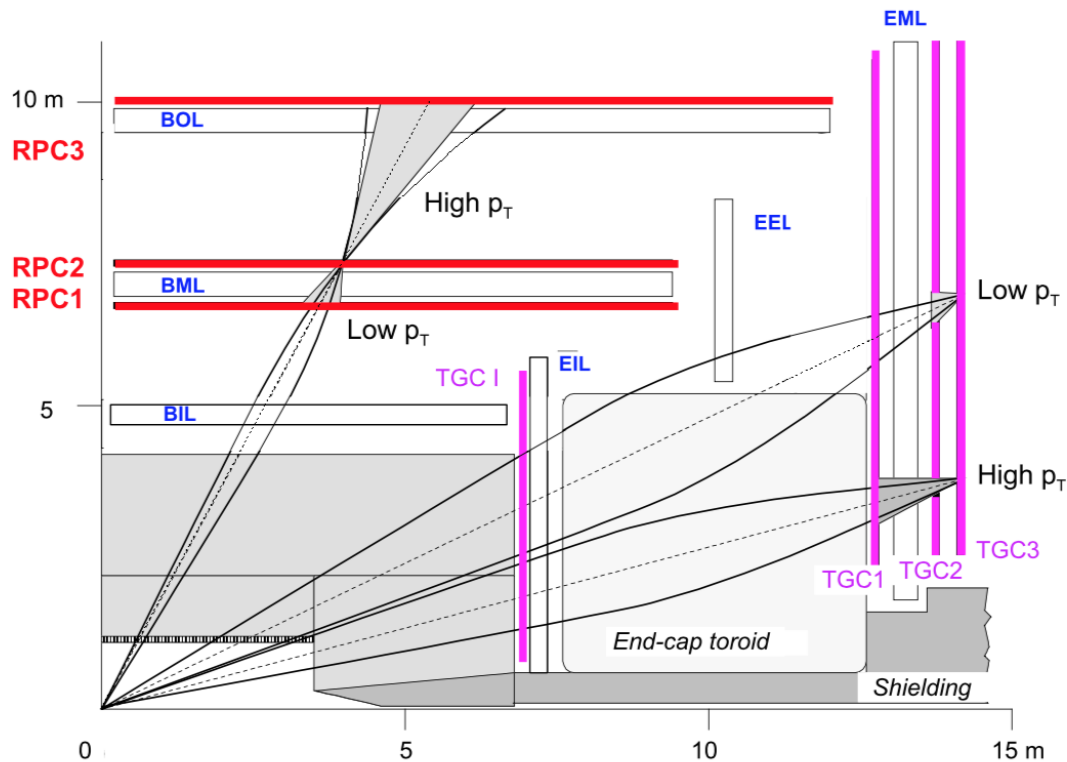


Figure 3.3: A schematic view of the L1Muon trigger chambers (from [51]).

857 3.3 High-Level Trigger

858 The events that are accepted by L1 are then buffered in the ROS and processed by the
 859 *High-Level Trigger* using information that is not available at L1, such as finer-granularity
 860 calorimeter inputs, precision measurements from the MS and tracking information from
 861 the ID. HLT receives RoI from L1 and performs the reconstruction within them. As
 862 needed, the reconstruction performed by the HLT software can either be run within RoIs
 863 or performing a so-called *full scan* of the detector. In order to reduce the processing time,
 864 a two-stage approach is employed for most HLT triggers: a first reconstruction (fast) to
 865 reject the majority of events; a second precision reconstruction for the remaining events
 866 (slower). Events that are accepted by the HLT get transferred to local storage at the exper-
 867 imental site and exported to the CERN’s computing centre for offline reconstruction [48].

868 3.3.1 Inner detector tracking

869 The track reconstruction in the Inner Detector is a vital component of the trigger decision
 870 in the HLT. A robust reconstruction of particle trajectories is an essential prerequisite for
 871 triggering on electrons, muons, taus, and b -jets. Furthermore, it is also used for triggering
 872 on inclusive pp interactions and for the online determination of the beamspot⁵ where the
 873 reconstructed tracks provide the input for vertex reconstruction.

⁵ The luminous region produced by the collisions of proton beams.

The ID tracking in the trigger also includes information from the IBL, which significantly improves the tracking performance and in particular the impact parameter resolution [41]. The tracking algorithms are called *Fast Tracking* and *Precision Tracking*. The former is comprised of trigger-specific pattern recognition algorithms, unlike the latter which is heavily based on offline-tracking algorithms. As already mentioned, once an **RoI** has been identified by **L1**, the algorithms are typically configured to run within it. Furthermore, in order to reduce CPU usage, the offline track-finding is seeded with tracks and space-points identified by fast tracking stage seeds. Running the full **HLT** reconstruction for each event on an individual node, affords the opportunity to better optimise the **RoI** geometry and use an advanced multi-stage strategy for the tau and b -jet triggers, which will be discussed in Section 3.3.2.

In order to reduce the detector volume of **RoI**, an advanced multi-stage approach, in particular for tau and b -jet tracking, is employed. The first stage is to identify leading tracks within a long-in- z but narrow-in- η and ϕ **RoI** running the Fast Track Finder (FTF) algorithm. The leading tracks are used to construct a second-stage **RoI**, constrained in both η and ϕ , but very tightly constrained in polar angle and with a small z position width. The FTF is then run again within the wider second-stage **RoI**, followed by the Precision Tracking [53]. The second stage, the Precision Tracking, is heavily based on an optimised subset of the tracking algorithms used offline, which is slower than the first but, in return, it identifies objects constructed starting from the inner detector tracks.

3.3.2 Performance of HLT

The performance of the tracking was estimated using 13-TeV pp collision collected in July 2015 by the **ATLAS** detector, unless otherwise stated. In order to be as unbiased as possible, specific monitoring triggers that do not require a track to be present for the event to be accepted are used to estimate the efficiency of the tracking algorithms. All the quantities used to estimate the performance of the tracking, i. e. efficiencies, residuals and resolutions, are calculated with respect to the tracks found by the offline reconstruction software. In particular, the efficiency is defined as the fraction of offline reference tracks that are matched to a trigger track

$$\mathcal{E} = \frac{N_{\text{trigger}}}{N_{\text{offline}}} \quad (3.1)$$

The tracking efficiency has been estimated for electrons and muons for the single-stage tracking, and for b -jets for the multi-stage approach, as part of the author's qualification task. The reconstructed tracks are required to have at least two (six) pixel (SCT) clusters and lie in the region $|\eta| < 2.5$. The closest trigger track within a cone of size $\Delta R = \Delta\eta^2 + \Delta\phi^2 = 0.05$ of the offline reconstructed track is selected as the matching trigger track.

909 Electrons

Figure 3.4 shows the tracking efficiency for the 24 GeV electron trigger as a function of η and p_T of the offline track. The tracking efficiency is measured with respect to off-line tracks with $p_T > 20$ GeV for tight offline electron candidates from the 24 GeV electron support trigger, which does not use the trigger tracks in the selection, despite being identical to the physics trigger. The FTF and Precision Tracking efficiencies are all above 99% within the whole pseudorapidity range. The small efficiency drop at low p_T is due to bremsstrahlung energy loss by electrons [48].

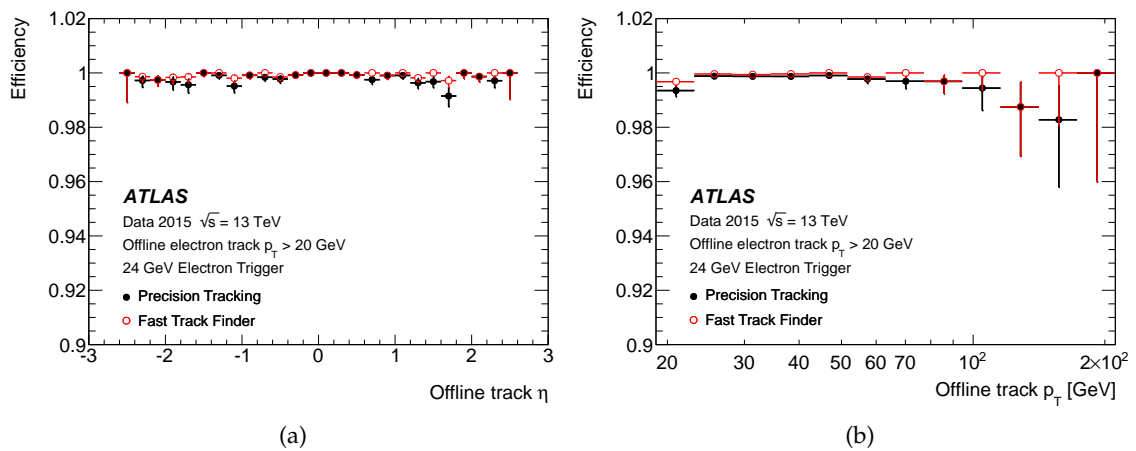


Figure 3.4: The ID tracking efficiency for the 24 GeV electron trigger is shown as a function of the (a) η and (b) p_T of the track of the offline electron candidate. Uncertainties based on Bayesian statistics are shown (from [48]).

917 Muons

Figure 3.5a shows the muon tracking performance with respect to offline muon candidates with $p_T > 6$ GeV selected by the 6 GeV muon support trigger as a function of the offline muon p_T . The efficiency is well above 99% in the entire p_T range for both FTF and Precision Tracking. Figure 3.5b shows the resolution of the transverse track impact parameter with respect to offline as a function of the offline muon p_T . FTF and Precision Tracking resolutions are better than 17 and 15 μm , respectively, for muon candidates with offline $p_T > 20$ GeV. The difference ($\sim 10\%$) between the two algorithms is driven by the fact that Precision Tracking (black solid points) uses the spacepoints found by the FTF (red open points), but refits them using the offline algorithm. In other words, Precision Tracking runs a faster version of the full offline track fit and it performs better.

928 ***b*-jets**

As previously mentioned, the b -jet triggers tracking algorithms are run in a larger ROI than for electrons or muons and in order to limit CPU usage, multiple stage track recon-

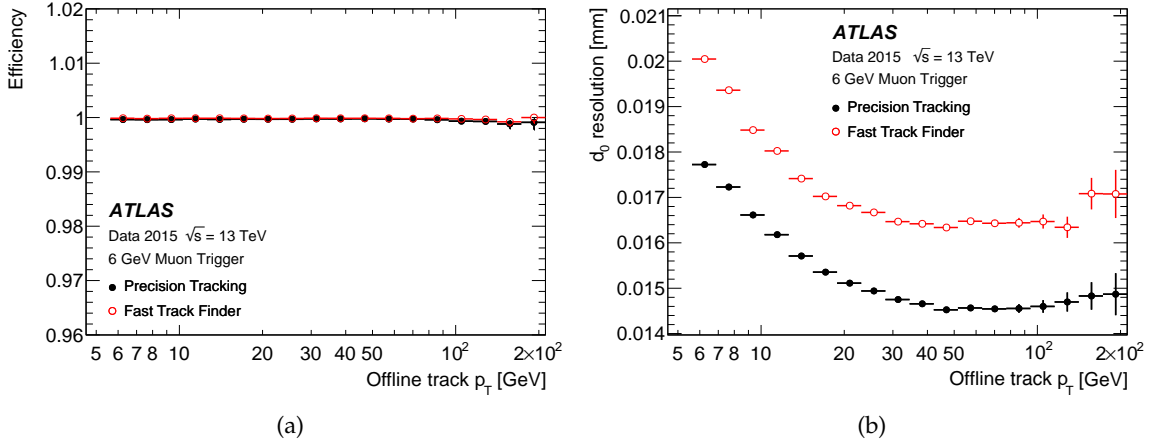


Figure 3.5: The ID tracking performance for the 6 GeV muon trigger; (a) efficiency as a function of the offline reconstructed muon p_T , (b) the resolution of the transverse impact parameter, d_0 as a function of the offline reconstructed muon p_T . Uncertainties based on Bayesian statistics are shown (from [48]).

931 construction was implemented and deployed during Run-2.

932 First, the leading track and its position along the beamline are determined by executing
 933 fast tracking in an ROI that is fully extended along the beamline, in the $|z| < 225$
 934 mm region, but narrow (0.1) in both η and ϕ , as shown in the blue-shaded region in
 935 Figure 3.6. The second stage is then run, using this position along the beamline, to recon-
 936 struct all tracks in an ROI that is larger (0.4) in both η and ϕ but limited to $|\Delta z| < 10$ mm
 937 with respect to the leading track, as shown by the green-shaded region in Figure 3.6.

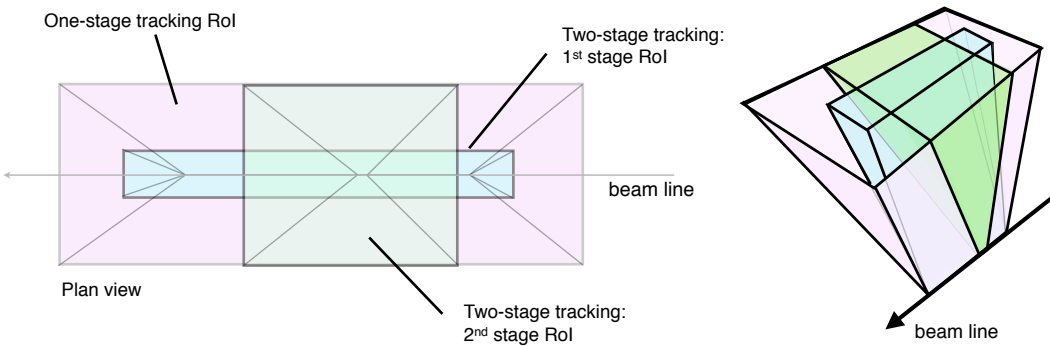


Figure 3.6: An illustration of the ROIs from the single-stage and two-stage tau lepton trigger tracking, shown in plan view (x-z plane) along the transverse direction and in perspective view. The z-axis is along the beam line. The combined tracking volume of the 1st and 2nd stage ROI in the two-stage tracking approach is significantly smaller than the ROI in the one-stage tracking scheme (from [48]).

938 The first-stage vertex tracking takes all jets identified by the jet trigger with $\eta > 30$
 939 GeV and reconstructs tracks with the FTF in a narrow region in η and ϕ around the jet
 940 axis for each jet, but with $|z| < 225$ mm along the beam line.

941 Following this step, the primary vertex reconstruction [54] is performed using the

tracks from the fast tracking stage. This vertex is used to define wider **RoIs** around the jet axes, with $|\Delta\eta| < 0.4$ and $|\Delta\phi| < 0.4$ but with $|\Delta z| < 20$ mm relative to the primary vertex z position. These **RoIs** are then used for the second-stage reconstruction that runs the fast track finder in the wider η and ϕ regions followed by the Precision Tracking, secondary vertexing and b -tagging algorithms, which will not be discussed in this work.

The performance of the primary vertexing in the b -jet vertex tracking can be seen in Figure 3.7a, which shows the vertex finding efficiency with respect to offline vertices in jet events with at least one jet with transverse energy above 55, 110, or 260 GeV and with no additional b -tagging requirement. The efficiency is shown as a function of the number of offline tracks with $p_T > 1$ GeV that lie within the boundary of the wider **RoI** (defined above) from the selected jets. The efficiency rises sharply and is above 90% for vertices with three or more tracks, and rises to more than 99.5% for vertices with five or more tracks. The resolution in z with respect to the offline z position as shown in Figure 3.7b is better than 100 μm for vertices with two or more offline tracks and improves to 60 μm for vertices with ten or more offline tracks.

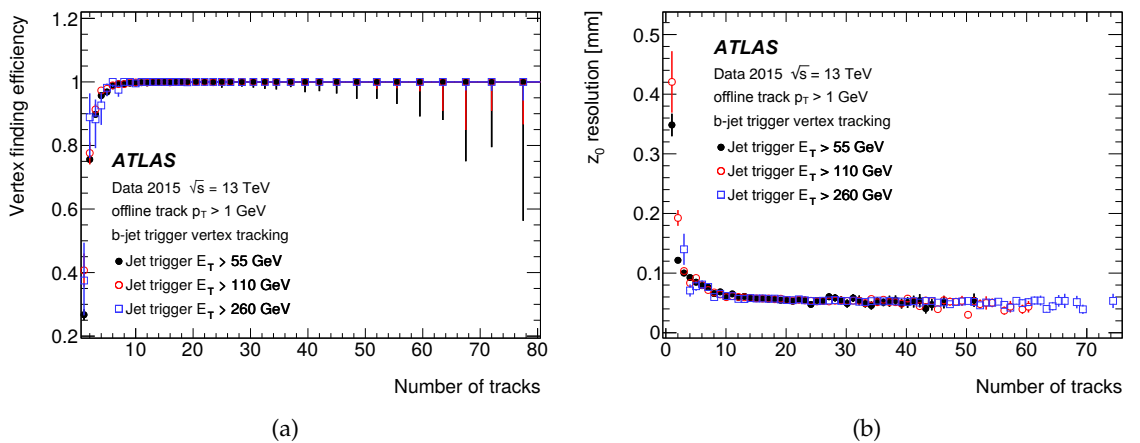


Figure 3.7: The trigger performance for primary vertices in the b -jet signatures for 55, 110 and 260 GeV jet triggers; (a) the vertexing efficiency as a function of the number of offline tracks within the jets used for the vertex tracking, (b) the resolution in z of the vertex with respect to the offline vertex position as a function of the number of offline tracks from the offline vertex (from [48]).

957 Missing Transverse Energy, E_T^{miss}

958 There exists several algorithms to reconstruct the E_T^{miss} at the **HLT**. The *missing H_T* ⁶ 959 (**MHT**) algorithm calculates E_T^{miss} as the negative sum of transverse energy of calibrated 960 jets, constructed from calibrated topological clusters of calorimeter cells. This algorithm 961 is the most relevant to the analysis presented in Chapter 5. The *cell algorithm* is based 962 on the negative sum of transverse energy deposited in calorimeter cells above a certain 963 noise threshold. Unlike the cell algorithm, which calculates E_T^{miss} on the electromagnetic

⁶ H_T is the scalar sum of the various p_T s in the event, $H_T = \sum_i p_T^i$.

scale, the MHT algorithm looks at jets calibrated using jet energy scale, so that numerical threshold values for similar signal efficiencies differ. *Pufit*, a third algorithm, was employed to disentangle calorimeter deposits from the hard-scatter, from those originating from pile-up interactions by grouping towers made out of topological clusters into a pile-up and a hard-scatter category. This grouping is based on their energy, where the threshold itself is dependent on the overall event activity measured by the total energy deposited in the calorimeter. The assumption is that the contribution to E_T^{miss} due to pile-up interactions is zero. Nevertheless a minimisation, which takes into account resolution terms, determines an effective energy density from pile-up interaction which allows a vanishing contribution to E_T^{miss} by the pile-up calorimeter towers. This correction is then subtracted from the hard-scatter towers. The negative sum of transverse energy of those pile-up corrected hard-scatter towers will provide the final E_T^{miss} value [55].

Figure 3.8 shows the turn-on curves for various E_T^{miss} triggers: Figure 3.8a shows the efficiency as a function of *modified*⁷ offline E_T^{miss} for three different E_T^{miss} trigger algorithms, using early 2016 pp collision data. The events have been selected using single lepton (electron or muon) triggers. The x-axis shows the offline E_T^{miss} calculated from the sum of electrons, photons and jets, without the contributions from the muons. Three different E_T^{miss} high-level trigger algorithms are shown: HLT_xe80_tc_lcw_L1XE50 calculates E_T^{miss} based on calibrated clusters of calorimeter cells, and has a threshold of 80 GeV. HLT_xe90_mht_L1XE50 calculates E_T^{miss} based on reconstructed jets, and it has a threshold of 90 GeV. HLT_xe100_L1XE50 calculates E_T^{miss} based on calorimeter cells calibrated at the electromagnetic scale, and has a threshold of 100 GeV. All three algorithms are seeded by a Level-1 trigger algorithm with a threshold of 50 GeV which is also shown; Figure 3.8b shows the combined L1 and HLT efficiency of the missing transverse energy triggers HLT_xe110_pufit_L1XE50 and HLT_xe110_mht_L1XE50 as well as the efficiency of the corresponding L1 trigger (L1_XE50) are shown as a function of the reconstructed E_T^{miss} (modified to count muons as invisible) using pp collision data collected in 2017. The events shown are taken from data with a $W \rightarrow \ell\nu$ selection to provide a sample enriched in real E_T^{miss} . The HLT E_T^{miss} of the *pufit* algorithm is calculated as the negative of the transverse momentum vector sum of all calorimeter topological clusters corrected for pileup. The pileup correction is done by grouping the clusters into coarser “towers” which are then marked as pileup if their E_T falls below a pileup-dependent threshold.

⁷ To calculate the E_T^{miss} efficiency, e.g. in events with muons, a muon trigger must be employed, therefore muon contributions are removed.

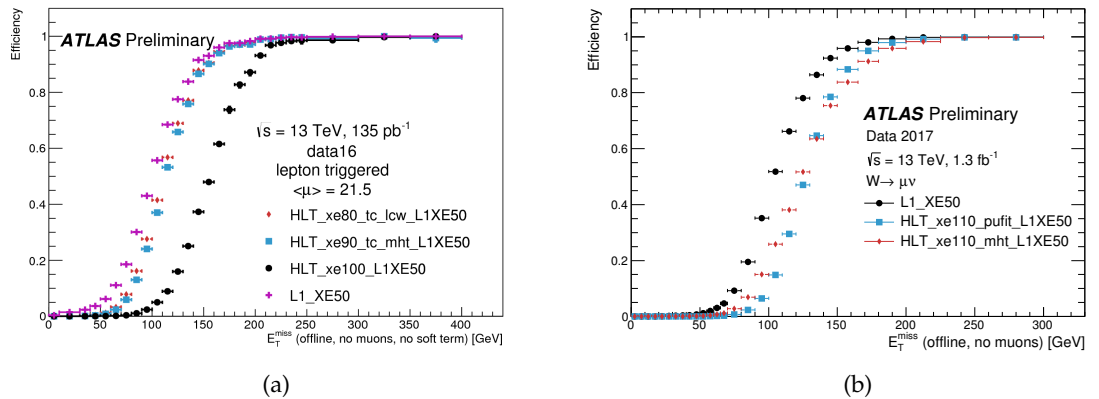


Figure 3.8: Turn-on curves of various E_T^{miss} triggers: Figure 3.8a shows the efficiency as a function of off-line E_T^{miss} for three different E_T^{miss} trigger algorithms. Three different E_T^{miss} high-level trigger algorithms are shown: HLT_xe80_tc_lcw_L1XE50 calculates E_T^{miss} based on calibrated clusters of calorimeter cells, and has a nominal threshold of 80 GeV. HLT_xe90_mht_L1XE50 calculates E_T^{miss} based on reconstructed jets, and has a nominal threshold of 90 GeV. HLT_xe100_L1XE50 calculates E_T^{miss} based on calorimeter cells calibrated at the electromagnetic scale, and has a nominal threshold (at the electromagnetic scale) of 100 GeV. All three algorithms are seeded by a Level-1 trigger algorithm with a nominal threshold of 50 GeV which is also shown; Figure 3.8b shows missing transverse energy trigger efficiencies for HLT_xe110_pufit_L1XE50 and HLT_xe110_mht_L1XE50 and for the corresponding L1 seed (L1_XE50). (from [56]).

996 **4 | Event Simulation and**
 997 **Object Reconstruction**

998

Nature isn't classical, dammit, and if you want to make a simulation of nature, you'd better make it quantum mechanical, and by golly it's a wonderful problem, because it doesn't look so easy.

Richard P. Feynman

999 The [ATLAS](#) software framework Athena [57], which is based on the Gaudi [58] frame-
 1000 work developed by [LHCb](#) [34], is used to reconstruct physics objects to be used by ana-
 1001 lysers, as the data collected and recorded by the [ATLAS](#) detector requires processing.
 1002 The Athena framework is capable of dealing with various aspects of the experiment soft-
 1003 ware, e. g. triggering or the processing of simulated data. Custom softwares, in particular
 1004 Monte Carlo ([MC](#)) simulations, are used to simulate physics events used to model back-
 1005 ground and signal process. These are produced through different stages, as shown in
 1006 Figure 4.1, the last of which produces an output with an analyser-friendly format.

1007 In this chapter the stages will be briefly explained as it follows: Event Generation
 1008 (Section 4.1) and the Detector Simulation (Section 4.1.1). The reconstruction of physics
 1009 objects¹, in both collected data and simulated [MC](#) events, will be described in Section 4.2.
 1010 Finally, a set of selection criteria are applied to reconstructed objects to identify those
 1011 suitable for use in analysis, as detailed in Section 4.3.

1012 **4.1 Generation of a MC-simulated event**

1013 [MC](#) event generators [60] are extensively used in particle physics to simulate [SM](#) and
 1014 [BSM](#) physics processes. A combination of perturbative and phenomenological calcula-
 1015 tions, to produce randomly distributed physics events, of a given type, with stable final

¹ A set of criteria needs to be applied in order to reconstruct the detected object as an “electron”, “photon”, “muon”, “jet”, etc.

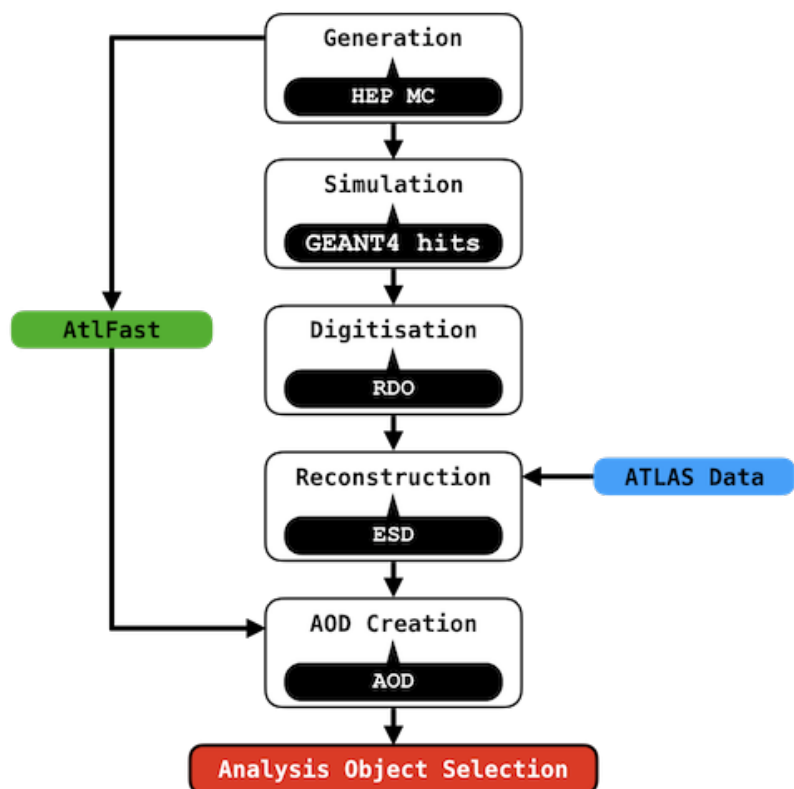


Figure 4.1: Illustration of the different stages of the workflow needed to produce analysable simulated and collected data outputs. The white boxes represent the processes, and their outputs are shown in black balloons: **RDO**, **ESD**, and the final product, **AOD**. The green ‘AtLFast’ box represents the alternative simulation method ATLFAST [59], discussed in Section 4.1.1. Finally, the blue box shows the stage at which the actual ATLAS data events begin processings.

state particles, is employed. As already mentioned in Chapter 2, The **ATLAS** detector collects pp - and heavy-ion-collisions data. When two protons collide at such high energy in the center of mass, the collision essentially occurs between the nucleon constituents: partons². Three valence quarks (uud), the gluons mediating the strong interactions between the valence quarks, and the sea quarks produced in virtual $q\bar{q}$ pairs due to interacting gluons, are included in the partons. Figure 4.2 shows one of these interactions which are known as Deep Inelastic Scattering (**DIS**) processes, simply because the substructure of the proton is probed, therefore *deep*, by an incoming particle, in this case a proton, whose momentum is not conserved in the process, therefore *inelastic*.

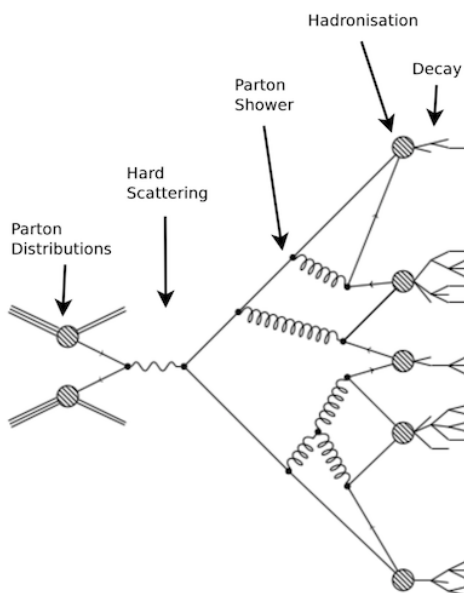


Figure 4.2: Example of a pp **DIS** event.

An important yet simplifying dimensionless physical quantity is the Bjorken scaling [63], which represents the fraction, x , of the proton momentum carried by an interacting parton. The measure of momentum transfer, Q^2 , in such events, is related to the momentum transferred by the exchanged boson, q , by $Q^2 = -q^2$. Parton Distribution Functions (**PDFs**) are used to describe mathematically the parton content of the colliding protons in order to model their interaction.

The pp scattering at the **LHC** can be categorised in processes such as *hard*, which can be described with perturbation theory, or *soft*, which involve non-perturbative **QCD** effects. Typically, a pp collision involves a hard scattering process between two partons, one for each proton, and a certain number of soft processes, such as Initial State Radiation (**ISR**), Final State Radiation (**FSR**), and Underlying Event (**UE**). The **ISR** involves

² “Feynman [61] interpreted the Bjorken scaling as the point-like nature of the nucleon’s constituents when they were incoherently scattered by the incident electron. Feynman named the point-like constituents partons. This is the parton model.”(taken from [62])

1036 particles, that are radiated by partons, which will interact in the hard process prior to
 1037 their scattering. Those partons, which are not involved in the hard scattering process, the
 1038 so-called *spectators*, form the **UE**. The **FSR** refers to particles that are radiated from the
 1039 final state products of the hard scattering. Furthermore, *parton showering* is a process in
 1040 which particles in the event that have colour can radiate gluons and/or produce $q\bar{q}$ pairs.
 1041 Products of these showers will undergo the process of *hadronisation* during which colour-
 1042 less hadron states are produced if Q^2 is of the order of 1 GeV. Such a process occurs due
 1043 to confinement.

1044 In order to allow analysers to select samples with relevant processes, **MC** samples are
 1045 divided in categories depending upon the hard-process specified before generation. It
 1046 is also possible to filter events to only produce a given final state, e.g. asking for zero
 1047 leptons, in order not to waste computational resources on events which would not pass
 1048 any selection criteria, regardless, improving the available statistics. The effect of the se-
 1049 lection will be taken into account by applying filter efficiency when the analysis is carried
 1050 out. The HEPMC format is used to store the output of simulated data outputs [64].

1051 **Parton Distribution Function** **PDFs** [65] mathematically describe the probability dens-
 1052 ity of constituent partons of the interacting protons to have a fraction, x , of the nucleon
 1053 momentum. They depend upon the parton type such as, valence quark, gluon, or sea
 1054 quark, and the momentum transfer Q^2 . Although perturbative calculations of the **PDFs**
 1055 are not feasible, the DGLAP [66, 67] evolution equations, using a range of hard scattering
 1056 data from both fixed target and collider experiments, can be used to estimate the depend-
 1057 ance as a function of Q^2 for a given parton. In other words, **PDFs** describe the evolution of
 1058 the structure functions of quarks and gluons as a function of the running³ strong coupling
 1059 constant α_s . Figure 4.3 shows the **PDFs**, calculated with input from HERA and CTEQ at
 1060 $Q^2 = 10 \text{ GeV}^2$ for up and down valence quarks, gluons, and sea-quarks.

1061 **Matrix Element** The matrix element is a simulation stage used to compute the hard
 1062 processes, where a large momentum transfer ($Q^2 > \mathcal{O}(1 \text{ GeV})$) is involved, which can
 1063 be calculated using quantum field theory techniques. Matrix elements to Leading Order
 1064 (**LO**) or Next-to-Leading Order (**NLO**) in an expansion in α_s , to calculate a probabilistic
 1065 distribution of the outgoing partons, are used to make **PDFs** simulate partons coming
 1066 into the hard scatter process. Hard emissions, namely the production of high momentum
 1067 quarks and gluons in the event, therefore processes such as, a gluon splitting into two
 1068 gluons, $g \rightarrow gg$, or a gluon decaying to a quark-antiquark pair $g \rightarrow q\bar{q}$, and a quark
 1069 radiating a gluon ($q \rightarrow qq$), can be added into the matrix element.

1070 **Parton Showers** The emission of extra soft objects cannot be modelled with the matrix
 1071 element, due to its non-perturbative nature. **PS** generators are instead used to include

³ Referred to a dependence on Q^2

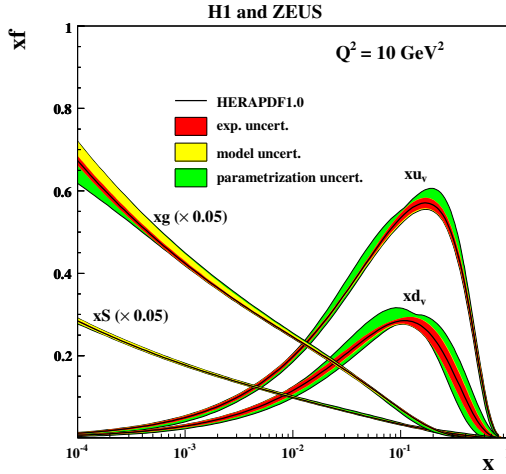


Figure 4.3: PDF from HERAPDF1.0, for up and down valence quarks xu_v and xd_v , gluons xg , and sea quarks $xS = 2x(\bar{U} + \bar{D})$, using a momentum transfer of $Q^2 = 10 \text{ GeV}^2$ (from [68]).

processes such as the emission of a gluon by a quark ($q \rightarrow qg$), or the emission of $q\bar{q}$ pairs $g \rightarrow qq$ or a gluon pair by a gluon $g \rightarrow gg$. HERWIG [69], PYTHIA [70], and SHERPA [71] collaborations have developed the most used PS models across the ATLAS community and beyond. Markov chains [72] are the heart of the algorithms used to simulate PS. These use probabilities that a gluon is radiated or a $q\bar{q}$ pair is produced.

At intermediate Q^2 , gluon/quark radiation may be treated as a hard emission or part of the PS, meaning that, in a given event double-counting might occur. To overcome such issue, the Catani-Krauss-Kuhn-Webber (CKKW) [73], and the Michelangelo L. Mangano (MLM) [74], schemes are employed to determine whether the emissions are part of the matrix element or PS. As the energy of the partons decrease below 1 GeV they will undergo hadronisation.

Hadronisation As previously mentioned in Section 1.1, once the quarks and gluons in the final state reach a Q^2 of the order of $\Lambda_{\text{QCD}} \sim 200 \text{ MeV}$, the recombination into colourless objects must occur. The modelling of the production of such bound state, the hadronisation, involves non-perturbative QCD and many more parameters than the parton showering. Phenomenological models, tuned using data, are then needed. The cluster model [75], used by HERWIG, and the Lund string model [76], used by PYTHIA, are the most employed.

Underlying Event Partons not involved in the hard process of the event, referred to as the UE [77], can lead to a certain number of soft interactions at a lower energy scale, therefore producing additional hadronic activity in the event. Once again, phenomenological models are used to account for such effect which is modelled within SHERPA and PYTHIA where a whole lot of additional free tuned-to-data parameters are included. More details can be found in [77].

1096 **4.1.1 Detector simulation**

1097 Although at this stage the output of the MC generators contains all the kinematic features
 1098 of the event, it is not yet possible to compare to the ATLAS collected data, as the inter-
 1099 actions of the particles passing through the detectors are not yet included. The GEANT4
 1100 software [78], included within the ATLAS offline software⁴, is used to simulate the en-
 1101 ergy deposited within the detector: a first stage is run to simulate the interactions of the
 1102 particles with the various sub-systems, and a second one is run to convert energy depos-
 1103 its into detector-output-like signals (voltage, times, etc.). This is the so-called *digitisation*.
 1104 The ouput is now produced with a format that is identical to the one produced by the
 1105 ATLAS TDAQ system, therefore MC and collected ATLAS data can now be consistently
 1106 processed by the same trigger and reconstruction softwares. Nonetheless, the ATLAS
 1107 Collaboration also use faster simulation software such as ATLFAST-II (AF2) [59] where,
 1108 in order to reduce the usage of the available computational resources, a parametrised
 1109 description of the showers in the calorimeters is implemented.

1110 **4.2 Object Reconstruction**

1111 At this stage both MC and data samples contain all the electronic pulses from the digitisa-
 1112 tion process. These have to be turned into tracks and calorimeter deposits which, in turn,
 1113 have to be processed to be reconstructed into physics object, such as electrons, photons,
 1114 muons, jets, taus, and missing energy, E_T^{miss} . Initially, a set of loose definitions is em-
 1115 ployed in order for various analyses to use such objects. Later, a set of tighter cuts can
 1116 be applied depending on what a particular analysis needs to focus on. This approach in-
 1117 creases the purity of the selected objects at the expense of selection efficiency. The criteria
 1118 used to define the physics objects, relevant to the analysis presented in this thesis, will be
 1119 presented in the following paragraphs.

1120 **Tracks and vertices** When a charged particle passes through the detector, all the ID sub-
 1121 systems, pixel, SCT and TRT components, register “hits” and then, tracing the particle’s
 1122 trajectory, the hits are reconstructed into a “track”. The most used algorithm is the so-
 1123 called *inside-out* method, whose clue is in the name: it works outwards from the center
 1124 of the ID to produce a track once it has initially grouped together hits in the pixel and
 1125 SCT sub-systems. If this track is then compatible with hits in the TRT detector, then these
 1126 hits are also included and the track is accepted. The back-tracking algorithm uses the
 1127 same approach, but in the opposite order, working from the TRT to the SCT and Pixel
 1128 detectors, and tracks can also be reconstructed using only the hits in the TRT.

1129 **Electrons**

⁴ All the software made available for analysers to be used after the data have been collected

1130 **Muons**

1131 **Photons**

1132 **Jets**

1133 **Missing Transverse Energy**

1134 **4.3 Object Selection**

1135 **4.3.1 Baseline Object Selection**

1136 **Leptons**

1137 **Photons**

1138 **Jets**

1139 **4.3.2 Overlap Removal**

1140 **4.3.3 Signal Object Selection**

1141 **Leptons**

1142 **Photons**

1143 **Jets**

1144 **5** | Stop searches in final states with
1145 jets and missing transverse en-
1146 ergy

1147 *In God we trust. All others must
bring data.*

W. Edwards Deming

1148 **6** | Results and Statistical Interpretations
1149

¹¹⁵⁰ **Appendix title**

¹¹⁵¹ Acronyms

- ¹¹⁵² **LHC** Large Hadron Collider
- ¹¹⁵³ **LEP** Large Electron-Positron Collider
- ¹¹⁵⁴ **CERN** European Organization for Nuclear Research
- ¹¹⁵⁵ **DM** Dark Matter
- ¹¹⁵⁶ **WIMP** Weakly Interacting Massive Particle
- ¹¹⁵⁷ **SUSY** Supersymmetry
- ¹¹⁵⁸ **GUT** Grand Unification Theory
- ¹¹⁵⁹ **RPC** *R*-Parity Conserving
- ¹¹⁶⁰ **RPV** *R*-Parity Violating
- ¹¹⁶¹ **LSP** Lightest Stable Particle
- ¹¹⁶² **NLSP** Next Lightest Supersymmetric Particle
- ¹¹⁶³ **FCNC** Flavour Changing Neutral Currents
- ¹¹⁶⁴ **MSSM** Minimal Supersymmetric Standard Model
- ¹¹⁶⁵ **pMSSM** Phenomenological [MSSM](#)
- ¹¹⁶⁶ **CKM** Cabibbo–Kobayashi–Maskawa
- ¹¹⁶⁷ **VEV** Vacuum Expectation Value
- ¹¹⁶⁸ **QFT** Quantum Field Theory
- ¹¹⁶⁹ **QCD** Quantum Chromo Dynamics
- ¹¹⁷⁰ **QED** Quantum Electrodynamics
- ¹¹⁷¹ **ATLAS** A Toroidal LHC ApparatuS
- ¹¹⁷² **ALICE** A Large Ion Collider Experiment

- ¹¹⁷³ **CMS** Compact Muon Solenoid
- ¹¹⁷⁴ **LHCb** Large Hadron Collider Beauty
- ¹¹⁷⁵ **TOTEM** TOTal cross section, Elastic scattering and diffraction dissociation
- ¹¹⁷⁶ Measurement at the [LHC](#)
- ¹¹⁷⁷ **LHCf** Large Hadron Collider forward
- ¹¹⁷⁸ **MoEDAL** Monopole & Exotics Detector At the [LHC](#)
- ¹¹⁷⁹ **IBL** Insertable B-Layer
- ¹¹⁸⁰ **SCT** SemiConductor Tracker
- ¹¹⁸¹ **TRT** Transition Radiation Tracker
- ¹¹⁸² **MS** Muon Spectrometer
- ¹¹⁸³ **ECAL** Electronic Calorimeter
- ¹¹⁸⁴ **HCAL** Hadronic Calorimeter
- ¹¹⁸⁵ **LAr** Liquid Argon
- ¹¹⁸⁶ **TDAQ** Trigger and Data Quality
- ¹¹⁸⁷ **LS1** Long Shutdown 1
- ¹¹⁸⁸ **LINAC2** Linear Accelerator 2
- ¹¹⁸⁹ **LINAC3** Linear Accelerator 3
- ¹¹⁹⁰ **LEIR** Low Energy Ion Ring
- ¹¹⁹¹ **BSM** Beyond Standard Model
- ¹¹⁹² **PSB** Proton Synchrotron Booster
- ¹¹⁹³ **PS** Proton Synchrotron
- ¹¹⁹⁴ **SPS** Super Proton Synchrotron
- ¹¹⁹⁵ **L1** Level-1
- ¹¹⁹⁶ **L1Calo** L1 Calorimeter
- ¹¹⁹⁷ **L1Muon** L1 Muon
- ¹¹⁹⁸ **L1Topo** Level-1 Topological
- ¹¹⁹⁹ **FTK** Fast TracKer

- 1200 **MDTs** Monitored Drift Tubes
1201 **CSCs** Cathode Strip Chambers
1202 **TGCs** Thin-Gap Chambers
1203 **RPCs** Resistive-Plate Chambers
1204 **ROS** Read-Out System
1205 **CTP** Central Trigger Processor
1206 **HLT** High Level Trigger
1207 **RoI** Region of Interest
1208 **ID** Inner Detector
1209 **SM** Standard Model
1210 **MC** Monte Carlo
1211 **RDO** Raw Data Object
1212 **ESD** Event Summary Data
1213 **AOD** Analysis Objects Data
1214 **DIS** Deep Inelastic Scattering
1215 **ISR** Initial State Radiation
1216 **FSR** Final State Radiation
1217 **UE** Underlying Event
1218 **PS** Parton Shower
1219 **PDFs** Parton Distribution Functions
1220 **CKKW** Catani-Krauss-Kuhn-Webber
1221 **MLM** Michelangelo L. Mangano
1222 **LO** Leading Order
1223 **NLO** Next-to-Leading Order

¹²²⁴ Bibliography

- ¹²²⁵ [1] M. Herrero, *The Standard Model*,. <https://arxiv.org/abs/hep-ph/9812242>.
¹²²⁶ [2](#)
- ¹²²⁷ [2] ATLAS Collaboration, *Observation of a New Particle in the Search for the Standard*
¹²²⁸ *Model Higgs Boson with the ATLAS Detector at the LHC*, *Phys.Lett.* **B716** (2012),
¹²²⁹ [arXiv:1207.7214 \[hep-ex\]](https://arxiv.org/abs/1207.7214). [2](#)
- ¹²³⁰ [3] CMS Collaboration, *Observation of a new boson at a mass of 125 GeV with the CMS*
¹²³¹ *experiment at the LHC*, *Phys.Lett.* **B716** (2012), [arXiv:1207.7235 \[hep-ex\]](https://arxiv.org/abs/1207.7235). [2](#)
- ¹²³² [4] M. E. Peskin, D. V. Schroeder, *An Introduction to Quantum Field Theory*. Westview
¹²³³ Press, 1995. [2](#)
- ¹²³⁴ [5] W. N. Cottingham and D. A. Greenwod, *An introduction to the standard model*.
¹²³⁵ Cambridge, 1998. [3](#)
- ¹²³⁶ [6] L. Lederman and C. Hill, *Symmetry and the Beautiful Universe*. Prometheus Books,
¹²³⁷ 2004. <https://books.google.co.uk/books?id=X2QPAQAAMAAJ>. [3](#)
- ¹²³⁸ [7] A. Pich, *The Standard Model of Electroweak Interactions*, [arXiv:1201.0537](https://arxiv.org/abs/1201.0537)
¹²³⁹ [hep-ph]. [4,6](#)
- ¹²⁴⁰ [8] K. A. Olive at al. (Particle Data Group), *Review of Particle Physics*, *Chin.Phys. C* **38(9)**
¹²⁴¹ (2014). [4](#)
- ¹²⁴² [9] S. Weinberg, *The quantum theory of fields. Vol. 2: Modern applications*. Cambridge
¹²⁴³ University Press, 2013. [5](#)
- ¹²⁴⁴ [10] S. L. Glashow, *Partial Symmetries of Weak Interactions*, *Nucl. Phys.* **22** (1961) 579–588.
¹²⁴⁵ [6](#)
- ¹²⁴⁶ [11] A. Salam and J. Ward, *Electromagnetic and weak interactions*, *Physics Letters* **13** no. 2,
¹²⁴⁷ (1964) 168 – 171. <http://www.sciencedirect.com/science/article/pii/0031916364907115>.
¹²⁴⁸ [6](#)

- 1250 [12] S. Weinberg, *A Model of Leptons*, *Phys. Rev. Lett.* **19** (1967) 1264–1266.
 1251 <https://link.aps.org/doi/10.1103/PhysRevLett.19.1264>. 6
- 1252 [13] P. W. Higgs, *Broken Symmetries and the Masses of Gauge Bosons*, *Phys. Rev. Lett.* **13**
 1253 (1964) 508–509. 7
- 1254 [14] J. Goldstone, A. Salam and S. Weinberg, *Broken Symmetries*, *Phys. Rev.* **127** (1962)
 1255 965–970. 7
- 1256 [15] ATLAS Collaboration, “Summary plots from the atlas standard model physics
 1257 group.” https://atlas.web.cern.ch/Atlas/GROUPS/PHYSICS/CombinedSummaryPlots/SM/ATLAS_a_SMSummary_TotalXsect/ATLAS_a_SMSummary_TotalXsect.png. 9
- 1260 [16] S. Weinberg, *Implications of Dynamical Symmetry Breaking*, *Phys. Rev. D* **19** (1976)
 1261 1277–1280. 8, 9
- 1262 [17] Super-Kamiokande Collaboration, Y. Fukuda et al., *Evidence for oscillation of
 1263 atmospheric neutrinos*, *Phys. Rev. Lett.* **81** (1998) 1562–1567,
 1264 [arXiv:hep-ex/9807003](https://arxiv.org/abs/hep-ex/9807003) [hep-ex]. 9
- 1265 [18] SNO Collaboration, *Measurement of the Rate of $\nu_e + d \rightarrow p + p + e^-$ Interactions
 1266 Produced by 8B Solar Neutrinos at the Sudbury Neutrino Observatory*, *Phys. Rev. Lett.*
 1267 **87** (2001). 9
- 1268 [19] T. O. W. of the Nobel Prize. https://www.nobelprize.org/nobel_prizes/physics/laureates/2015/. 9
- 1270 [20] E. Kh. Akhmedov, et. al, *Seesaw mechanism and structure of neutrino mass matrix*,
 1271 *Phys. Lett.* **B478** (1999). 10
- 1272 [21] V. C. Rubin and W. K. Ford, Jr., *Rotation of the Andromeda Nebula from a Spectroscopic
 1273 Survey of Emission Regions*, *Astrophysical Journal* **159** (1970) 379. 10
- 1274 [22] M. H. Jones, R. J. A. Lambourne, and S. Serjeant, *An Introduction to Galaxies and
 1275 Cosmology* (2nd ed). Cambridge University Press/Open University, Cambridge,
 1276 January, 2015. <http://oro.open.ac.uk/44361/>. 10
- 1277 [23] S. P. Martin, *A Supersymmetry primer*, [arXiv:hep-ph/9709356](https://arxiv.org/abs/hep-ph/9709356) [hep-ph]. [Adv.
 1278 Ser. Direct. High Energy Phys.18,1(1998)]. 10
- 1279 [24] R. Barbieri and G. F. Giudice, *Upper Bounds on Supersymmetric Particle Masses*, *Nucl.
 1280 Phys.* **B306** (1988) 63–76. 10
- 1281 [25] F. Jegerlehner, *The hierarchy problem of the electroweak Standard Model revisited*,
 1282 [arXiv:1305.6652](https://arxiv.org/abs/1305.6652) [hep-ph]. 12

- 1283 [26] H. E. Haber and G. L. Kane, *The Search for Supersymmetry: Probing Physics Beyond the*
 1284 *Standard Model*, Phys. Rept. **117** (1985) 75–263. 14
- 1285 [27] K. Hidaka and A. Bartl, *Impact of bosonic decays on the search for the lighter stop and*
 1286 *sbottom squarks*, Phys. Lett. **B501** (2001) 78–85, arXiv:hep-ph/0012021
 1287 [hep-ph]. 14
- 1288 [28] C. Borschensky, M. Krämer, A. Kulesza, M. Mangano, S. Padhi, T. Plehn, and
 1289 X. Portell, *Squark and gluino production cross sections in pp collisions at $\sqrt{s} = 13, 14, 33$*
 1290 *and 100 TeV*, Eur. Phys. J. **C74** no. 12, (2014) 3174, arXiv:1407.5066 [hep-ph].
 1291 16
- 1292 [29] O. S. Brüuning, P. Collier, P. Lebrun, S. Myers, R. Ostojic, J. Poole and P. Proudlock,
 1293 *LHC Design Report*, <https://cds.cern.ch/record/782076>. 19, 20
- 1294 [30] J.M. Jowett, M. Schaumann, R. Alemany, R. Bruce, M. Giovannozzi, P. Hermes, W.
 1295 Hofle, M. Lamont, T. Mertens, S. Redaelli, J. Uythoven, J. Wenninger, *The 2015*
 1296 *Heavy-Ion Run of the LHC*, [http://accelconf.web.cern.ch/accelconf/](http://accelconf.web.cern.ch/accelconf/ipac2016/papers/tupmw027.pdf)
 1297 ipac2016/papers/tupmw027.pdf. 20
- 1298 [31] C. Lefèvre, *The CERN accelerator complex*,
 1299 <http://cds.cern.ch/record/1260465>. 21, 22
- 1300 [32] ATLAS Collaboration, *The ATLAS experiment at the CERN Large Hadron Collider*,
 1301 Journal of Instrumentation **3** no. 08, (2008) S08003.
 1302 <http://stacks.iop.org/1748-0221/3/i=08/a=S08003>. 21, 23, 29, 33, 34
- 1303 [33] CMS Collaboration, *The CMS experiment at the CERN LHC*, Journal of
 1304 Instrumentation **3** no. 08, (2008) S08004.
 1305 <http://stacks.iop.org/1748-0221/3/i=08/a=S08004>. 21
- 1306 [34] LHCb Collaboration, et. al, *The LHCb Detector at the LHC*, JINST (2008). 21, 42
- 1307 [35] ALICE Collaboration, *The ALICE experiment at the CERN LHC*, Journal of
 1308 Instrumentation **3** no. 08, (2008) S08002.
 1309 <http://stacks.iop.org/1748-0221/3/i=08/a=S08002>. 21
- 1310 [36] T. T. Collaboration, *The TOTEM Experiment at the CERN Large Hadron Collider*,
 1311 Journal of Instrumentation **3** no. 08, (2008) S08007.
 1312 <http://stacks.iop.org/1748-0221/3/i=08/a=S08007>. 21
- 1313 [37] L. Collaboration. 21
- 1314 [38] J. Pinfold, *The MoEDAL experiment at the LHC*, EPJ Web Conf. **145** (2017) 12002. 21

- 1315 [39] A. Yamamoto, Y. Makida, R. Ruber, Y. Doi, T. Haruyama, F. Haug, H. ten Kate,
 1316 M. Kawai, T. Kondo, Y. Kondo, J. Metselaar, S. Mizumaki, G. Olesen, O. Pavlov,
 1317 S. Ravat, E. Sbrissa, K. Tanaka, T. Taylor, and H. Yamaoka, *The ATLAS central
 1318 solenoid*, *Nuclear Instruments and Methods in Physics Research Section A:
 1319 Accelerators, Spectrometers, Detectors and Associated Equipment* **584** no. 1, (2008)
 1320 **53 – 74.** [http://www.sciencedirect.com/science/article/pii/
 1321 S0168900207020414](http://www.sciencedirect.com/science/article/pii/S0168900207020414). **23, 24**
- 1322 [40] ATLAS Collaboration, *The ATLAS Inner Detector commissioning and calibration*, *Eur.
 1323 Phys. JC* **70**, [arXiv:1004.5293](https://arxiv.org/abs/1004.5293). **24**
- 1324 [41] ATLAS Collaboration, *ATLAS Insertable B-Layer Technical Design Report.*,
 1325 <https://cds.cern.ch/record/1291633>. **25, 36**
- 1326 [42] G. A. et al., *ATLAS pixel detector electronics and sensors*, *Journal of Instrumentation* **3**
 1327 no. 07, (2008) P07007.
 1328 <http://stacks.iop.org/1748-0221/3/i=07/a=P07007>. **25**
- 1329 [43] A. Bingül, *The ATLAS TRT and its Performance at LHC*, *Journal of Physics:
 1330 Conference Series* **347** no. 1, (2012) 012025. [http://iopscience.iop.org/
 1331 article/10.1088/1742-6596/347/1/012025/meta](http://iopscience.iop.org/article/10.1088/1742-6596/347/1/012025/meta). **26**
- 1332 [44] T. A. Collaboration, *Studies of the performance of the ATLAS detector using cosmic-ray
 1333 muons*, *The European Physical Journal C* **71** no. 3, (2011) 1593.
 1334 <https://doi.org/10.1140/epjc/s10052-011-1593-6>. **27**
- 1335 [45] ATLAS Collaboration, *ATLAS liquid-argon calorimeter: Technical Design Report.*,
 1336 <https://cds.cern.ch/record/331061>. **28**
- 1337 [46] ATLAS Collaboration, *ATLAS muon spectrometer: Technical design report.*,
 1338 <https://cds.cern.ch/record/331068>. **29**
- 1339 [47] ATLAS Collaboration, *Fast TracKer (FTK) Technical Design Report.*,
 1340 <https://cds.cern.ch/record/1552953>. **30**
- 1341 [48] A. Collaboration, *Performance of the ATLAS Trigger System in 2015*, *Eur. Phys. J. C* **77**
 1342 (2017), [arXiv:1611.09661 \[hep-ex\]](https://arxiv.org/abs/1611.09661). **32, 33, 35, 37, 38, 39**
- 1343 [49] E. Simoni, *The Topological Processor for the future ATLAS Level-1 Trigger: from design to
 1344 commissioning*, [arXiv:1406.4316](https://arxiv.org/abs/1406.4316). **33**
- 1345 [50] ATLAS Collaboration, *The ATLAS Level-1 Calorimeter Trigger*, *Journal of
 1346 Instrumentation* **3** no. 03, (2008) P03001.
 1347 <http://stacks.iop.org/1748-0221/3/i=03/a=P03001>. **33**

- 1348 [51] ATLAS Collaboration, *Performance of the ATLAS Trigger System in 2010*, Eur. Phys. J
 1349 **C72** (2012), [arXiv:1110.1530 \[hep-ex\]](https://arxiv.org/abs/1110.1530). 34, 35
- 1350 [52] ATLAS Collaboration, *Expected Performance of the ATLAS Experiment - Detector,
 1351 Trigger and Physics*, [arXiv:0901.0512 \[hep-ex\]](https://arxiv.org/abs/0901.0512). 33
- 1352 [53] ATLAS Collaboration, F. Miano, *The design and performance of the ATLAS Inner
 1353 Detector trigger for Run 2 LHC collisions at $\sqrt{s} = 13$ TeV*, PoS **ICHEP2016** (2016) 856.
 1354 36
- 1355 [54] ATLAS Collaboration, *Performance of primary vertex reconstruction in proton-proton
 1356 collisions at $\sqrt{s} = 7$ TeV in the ATLAS experiment*, Tech. Rep. ATLAS-CONF-2010-069,
 1357 CERN, Geneva, Jul, 2010. <http://cds.cern.ch/record/1281344>. 38
- 1358 [55] N. Ruthmann, Y. Nakahama, and C. Leonidopoulos, *Trigger Menu in 2016*, Tech.
 1359 Rep. ATL-COM-DAQ-2016-137, CERN, Geneva, Sep, 2016.
 1360 <https://cds.cern.ch/record/2216366>. 40
- 1361 [56] ATLAS Collaboration, “Missing energy trigger public results.”
 1362 [https://twiki.cern.ch/twiki/bin/view/AtlasPublic/
 1363 MissingEtTriggerPublicResults](https://twiki.cern.ch/twiki/bin/view/AtlasPublic/MissingEtTriggerPublicResults). 41
- 1364 [57] ATLAS Collaboration, *ATLAS Computing : technical design report*,
 1365 <https://cds.cern.ch/record/837738>. 42
- 1366 [58] G. Barrand, et. al, *GAUDI - A software architecture and framework for building HEP
 1367 data processing applications*,
 1368 [https://dx.doi.org/10.1016/S0010-4655\(01\)00254-5](https://dx.doi.org/10.1016/S0010-4655(01)00254-5). 42
- 1369 [59] W. Lukas, *Fast Simulation for ATLAS: Atlfast-II and ISF*, J. Phys.: Conf. Ser **396**
 1370 no. 022031, (2012). 43, 47
- 1371 [60] A. Buckley et al., *General-purpose event generators for LHC physics*, Phys. Rept. **504**
 1372 (2011) 145–233, [arXiv:1101.2599 \[hep-ph\]](https://arxiv.org/abs/1101.2599). 42
- 1373 [61] R. P. Feynman, *Very High-Energy Collisions of Hadrons*, Phys. Rev. Lett. **23** (1969)
 1374 1415–1417. <https://link.aps.org/doi/10.1103/PhysRevLett.23.1415>.
 1375 44
- 1376 [62] T.-M. Yan and S. D. Drell, *The Parton Model and its Applications*, Int. J. Mod. Phys.
 1377 **A29** (2014) 0071, [arXiv:1409.0051 \[hep-ph\]](https://arxiv.org/abs/1409.0051). 44
- 1378 [63] J. D. Bjorken, *Asymptotic Sum Rules at Infinite Momentum*, Phys. Rev. **179** (1969)
 1379 1547–1553. <https://link.aps.org/doi/10.1103/PhysRev.179.1547>. 44

- 1380 [64] M. Dobbs and J. B. Hansen, *The HepMC C++ Monte Carlo event record for High Energy*
 1381 *Physics*, Computer Physics Communications **134** no. 1, (2001) 41 – 46. [http://
 1382 www.sciencedirect.com/science/article/pii/S0010465500001892](http://www.sciencedirect.com/science/article/pii/S0010465500001892).
- 1383 **45**
- 1384 [65] J. M. Campbell, J. Houston and W. Stirling, *Hard Interactions of Quarks and Gluons: A*
 1385 *Primer of LHC Physics*, Rept. Prog. Phys **70** no. 1, (2007). **45**
- 1386 [66] V. N. Gribov and L. N. Lipatov, *Deep inelastic e p scattering in perturbation theory*, Sov.
 1387 J. Nucl. Phys. **15** (1972) 438–450. [Yad. Fiz.15,781(1972)]. **45**
- 1388 [67] G. Altarelli and G. Parisi, *Asymptotic Freedom in Parton Language*, Nucl. Phys. **B126**
 1389 (1977) 298–318. **45**
- 1390 [68] ZEUS, H1 Collaboration, F. D. Aaron et al., *Combined Measurement and QCD*
 1391 *Analysis of the Inclusive e+ - p Scattering Cross Sections at HERA*, JHEP **01** (2010) 109,
 1392 [arXiv:0911.0884 \[hep-ex\]](https://arxiv.org/abs/0911.0884). **46**
- 1393 [69] G. Corcella, et al., *HERWIG 6: an event generator of hadron emission reactions with*
 1394 *interfering gluons (including supersymmetric processes)*, J. High Energy Phys.
 1395 **JHEP(2001)** (2001). [http://iopscience.iop.org/article/10.1088/
 1396 1126-6708/2001/01/010/meta](http://iopscience.iop.org/article/10.1088/1126-6708/2001/01/010/meta). **46**
- 1397 [70] T.S., et al., *PYTHIA 6.4 physics and manual*, J. High Energy Phys. **JHEP(2006)** (2006).
 1398 [http://iopscience.iop.org/article/10.1088/1126-6708/2006/05/
 1399 026/meta](http://iopscience.iop.org/article/10.1088/1126-6708/2006/05/026/meta). **46**
- 1400 [71] T. Gleisberg et al., *Event generation with SHERPA 1.1*, JHEP **02** (2009) 007. **46**
- 1401 [72] Bernd A. Berg, *Introduction to Markov Chain Monte Carlo Simulations and their*
 1402 *Statistical Analysis*, [arXiv:cond-mat/0410490 \[cond-mat\]](https://arxiv.org/abs/cond-mat/0410490). **46**
- 1403 [73] S. Catani, F. Krauss, R. Kuhn and B. Webber, *QCD Matrix Elements + Parton Showers*,
 1404 **JHEP 0111** (2001), [arXiv:hep-ph/0109231 \[hep-ph\]](https://arxiv.org/abs/hep-ph/0109231). **46**
- 1405 [74] M. L. Mangano, M. Moretti and R. Pittau, *Multijet Matrix Elements and Shower*
 1406 *Evolution in Hadronic Collisions: Wb̄ + n Jets as a Case Study*, Nucl.Phys **B632** (2001),
 1407 [arXiv:0108069 \[hep-ph\]](https://arxiv.org/abs/hep-ph/0108069). **46**
- 1408 [75] A. Kupco , *Cluster Hadronization in HERWIG 5.9*, [arXiv:hep-ph/9906412](https://arxiv.org/abs/hep-ph/9906412)
 1409 [\[hep-ph\]](https://arxiv.org/abs/hep-ph/9906412). **46**
- 1410 [76] B. Andersson, S. Mohanty and F. Soderberg, *Recent Developments in the Lund Model*,
 1411 [arXiv:hep-ph/0212122 \[hep-ph\]](https://arxiv.org/abs/hep-ph/0212122). **46**
- 1412 [77] R. D. Field, *The Underlying Event in Hard Scattering Processes*,
 1413 [arXiv:hep-ph/0201192 \[hep-ph\]](https://arxiv.org/abs/hep-ph/0201192). **46**

-
- ¹⁴¹⁴ [78] GEANT4 Collaboration, *Geant4 a simulation toolkit*, [Nucl. Instrum. Meth. A 506](#)
¹⁴¹⁵ [\(2003\). 47](#)